

Contents lists available at [ScienceDirect](https://www.sciencedirect.com)

Remote Sensing of Environment

journal homepage: www.elsevier.com/locate/rse

Sub-continental-scale mapping of tidal wetland composition for East Asia: A novel algorithm integrating satellite tide-level and phenological features

Zhen Zhang^{a,b}, Nan Xu^c, Yangfan Li^{a,b,*}, Yi Li^{a,b}^a State Key Laboratory of Marine Environmental Science, Key Laboratory of Coastal and Wetland Ecosystems (Ministry of Education), College of the Environment and Ecology, Xiamen University, Xiamen 361102, China^b Southern Marine Science and Engineering Guangdong Laboratory (Zhuhai), Zhuhai 519080, China^c College of Marine Science and Engineering, Nanjing Normal University, Nanjing 210023, China

ARTICLE INFO

Editor: Dr. Marie Weiss

Keywords:

Image compositing
Phenology
Mangroves
Salt marsh
Tidal flats
Sentinel-2
Coastline
Google Earth Engine

ABSTRACT

Tidal wetlands, the global hotspots of biodiversity and carbon stocks, are currently experiencing widespread modifications in their composition due to human disturbances and changing climate. Accurate mapping of tidal wetland composition is crucial and urgently required for the conservation and management of coastal ecosystem, as well as for maximizing their associated services. However, remote sensing of tidal wetlands is still challenge due to periodic tidal fluctuations, frequent cloud cover, and similar spectral characteristics with terrestrial land-cover types. Previous approaches to mapping the tidal wetlands have been restricted to small study regions or have focused on an individual tidal wetland type, thus limiting their ability to consistently monitor the composition of tidal wetlands over large geographic extents. To address the above issues, we proposed a novel algorithm on Google Earth Engine, called Multi-class Tidal Wetland Mapping by integrating Tide-level and Phenological features (MTWM-TP), to simultaneously map mangroves, salt marshes and tidal flats for specifying large-scale tidal wetland composition. The MTWM-TP algorithm firstly generates several noise-free composite images with different tide levels and phenological stages and then concatenates them into a random forest classifier for further classification. The usage of tide-level and phenological features eliminates inland landscapes and help to distinguish deciduous salt marshes and evergreen mangroves, leading to a statistically significant improvement in accuracy. We applied the algorithm to 10,274 Sentinel-2 images of East Asia and derived a 10-m-resolution multi-class tidal wetland map with an overall accuracy of 97.02% at a sub-continental scale. We found that tidal wetlands occupied 1,308,241 ha of areas in East Asia in 2020, of which 89.12% were tidal flats, 9.39% were salt marshes, and only 1.49% were mangroves. This spatially explicit map of tidal wetland composition will provide valuable guidance for coastal biodiversity protection and blue carbon restoration. In addition, the proposed MTWM-TP algorithm can serve as a reliable means for monitoring sub-continental- or larger-scale tidal wetland composition more broadly.

1. Introduction

Tidal wetlands, composing of unvegetated tidal flats, mangroves, and salt marshes (Turpie et al., 2015; Yang et al., 2008), play a unique role in linking terrestrial and marine environments, providing numerous crucial ecosystem services such as coastal protection, fishery enhancement, and carbon sequestration to people (Barbier et al., 2011). Despite their small portion of the Earth's surface (<0.5%), tidal wetlands are widely distributed in diverse climate zones and are among the most productive ecosystems on the planet (Donato et al., 2011), storing a

large amount of carbon (10–24 Pg C globally) (Duarte et al., 2013). However, at the same time tidal wetlands are one of the most fragile ecosystems worldwide, severely threatened by disturbance from climate change, which triggers extensive variation of tidal wetland composition (TWC). For example, decreased frost frequency and precipitation resulted in mangroves encroached into salt marshes (Cavanaugh et al., 2014; Saintilan et al., 2014) and transferred salt marshes to unvegetated tidal flats (Osland et al., 2016). Climate-induced sea-level rise is also likely to alter the TWC by changing the flood frequency and inundation depth (Nicholls and Cazenave, 2010; Kirwan et al., 2016). In turn,

* Corresponding author at: State Key Laboratory of Marine Environmental Science, Key Laboratory of Coastal and Wetland Ecosystems (Ministry of Education), College of the Environment and Ecology, Xiamen University, Xiamen 361102, China.

E-mail address: yangf@xmu.edu.cn (Y. Li).

<https://doi.org/10.1016/j.rse.2021.112799>

Received 14 June 2021; Received in revised form 7 October 2021; Accepted 10 November 2021

Available online 22 November 2021

0034-4257/© 2021 Elsevier Inc. All rights reserved.

changes in TWC will cause alterations of habitats for some migratory shorebirds and the native species that inhabit stable tidal wetland mosaic (Kelleway et al., 2017) and affect the carbon cycle of the coastal environments (Lovell and Reef, 2020). As a result, dynamic monitoring of TWC at a large scale is pivotal for accounting for coastal carbon sequestration, understanding the changes of coastal habitats, and for broadly protecting sensitive coastal ecosystems under changing climate.

Remote sensing techniques offer a cost-effective way to continuously detect TWC over large geographic extents and long historic periods. However, they are more challenging in detecting tidal wetlands than terrestrial landscapes due to the highly dynamic intertidal environment. The remotely-detected spatial extent of tidal wetlands is greatly impacted by the tidal stage at the time of remote sensing data capture (O'Connell et al., 2017; Sun et al., 2021). The use of low-tide images thus is necessary to capture the moment of tidal wetland exposure and detect the entire spatial extent. On the other hand, frequent cloud cover in the coastal area, particularly tropical and subtropical regions, reduces the likelihood of acquiring clear-sky low-tide images. Even with cloud-free low-tide imagery, similar spectral characteristics of tidal wetlands and terrestrial landscapes such as terrestrial vegetation and bare soils can also hinder accurate classification. These challenges could be addressed at the local scale by using high-accuracy Light Detection and Ranging (LiDAR) topographic mapping, sub-meter remote sensing images like World-View 2 imagery, and field measurements of tidal stages (e.g., Campbell and Wang, 2018), but are still prevailing for those large-scale studies that can only acquire moderate-resolution satellite remote sensing data like Landsat or Sentinel imagery with a long revisiting period. In such a situation, it is critical to develop efficient and general algorithms to account for tidal fluctuations, cloud contamination, and spectral similarity.

Since visual tidal differences among satellite images are evident, with lower tides exhibit more visible vegetated wetlands and tidal flats, a straightforward way to deal with tidal fluctuations and cloud coverage is to manually collect cloud-free low-tide scenes (e.g., Gu et al., 2021; Jia et al., 2018). There are also precedents (Rogers et al., 2017; Murray et al., 2012) for automatically collecting the most suitable low-tide scenes using the estimated tidal height from tide models. Additionally, to overcome the issue of similar spectral characteristics, several studies (Chen et al., 2017; Lopes et al., 2020) manually delineated accurate shorelines as a pre-processing step to excluded inland areas. Nonetheless, these strategies can be too labor-intensive and time-consuming to apply at a national or larger scale. More importantly, the inherent limitation of these, and any method which utilizes single-date scenes, is the requirement for cloud-free satellite images during low tide, which may be unavailable for many regions where cloud coverage is frequent.

With advances in computation resources like Google Earth Engine (GEE) (Gorelick et al., 2017), several recent studies used multi-temporal instead of single-date images into tidal wetland mapping to address the three challenges above (Wang et al., 2019). Based on multi-tidal remotely-sensed imagery, tidal variations were considered as an essential feature rather than a barrier to separate tidal wetlands from terrestrial landscapes because only the spectral characteristics of tidal wetlands vary with tide levels (Rogers et al., 2017; Taddeo et al., 2019). Image compositing methods, which select the best pixels for each pixel location from an image stack, were widely used in these studies to generate cloud-free composite images with different tidal inundation status. Image compositing allows exploiting all imagery, including partially cloudy images, thus is particularly suitable for moderate-resolution optical sensors like Sentinel-2 (S2) which provide detailed spatial information but lack sufficient cloud-free observations. For instance, Sagar et al. (2017) generated a median composite of Normalized Difference Water Index (NDWI) in each tidal stage interval to delineate the intertidal extent of Australia based on a full time-series of Landsat observations. Another milestone of mapping tidal wetlands through composite images is Murray et al. (2019), who extracted the global distribution of tidal flats by using several quantile composite

images representing different tidal stages. However, their methods do not capture the highest and lowest tide conditions, thus omitting marginal tidal wetlands. By developing the quantile composite method, Zhao et al. (2020) used the 95th and 5th quantiles at each pixel of the image stack to obtain the lowest and highest tide composite images, respectively. This strategy was followed by a more recent work in mapping tidal flats of China (Jia et al., 2021) with a difference that using maximum instead of quantiles to composite images (i.e., using Maximum Value Composite method, MaxVC). A key limitation of these compositing methods, however, is that they are highly sensitive to image noise, such as residual cloud cover even after the cloud-masking procedure (Coluzzi et al., 2018), and spectral reflectance outliers caused by atmosphere correction or sensor miscalibration. Due to the use of the full image stack without any filter procedure, any noise in the image stack would interfere with the order of pixel values and thus caused abnormal quantile (or maximum) value. As such, a robust method for compositing images with different tide levels ranging from highest to lowest is required to help better use tide-level features in the classification procedures.

Phenology is an essential feature considered to classify vegetated tidal wetlands. Some studies have proposed selecting key dates representing appropriate phenological windows to provide extra features in tidal wetland classification (Tian et al., 2020; Valderrama-Landeros et al., 2021). For example, Tian et al. (2020) monitored the invasion processes of *Spartina alterniflora*, an invasive salt marsh species in China, by combining images during the growing season (154–270th days) and dormant season (1–142th days). However, since the key phenological dates vary with species and can vary in spatial and temporal domain even within the same species (Caparros-Santiago et al., 2021), uncertainties would arise in the final classification results if applying the same key dates to different study regions or periods. Considering these specificities, we need to develop an automated method without dependence on prior knowledge about exact phenological dates.

There are several existing global tidal wetland products, including the global mangrove extent for the year 2000 (Giri et al., 2011), global mangrove extent from 2000 to 2012 (Hamilton and Casey, 2016), global mangroves from 1996 to 2016 (Bunting et al., 2018), and global tidal flats from 1984 to 2016 (Murray et al., 2019). While these global products and the above-mentioned regional works provided valuable resources for understanding tidal wetlands, most of them were developed for an individual wetland type. As each type was mapped separately with different data sources, classification methodologies, training samples and interpreters, errors in each map would be accumulated in the final multi-class map (Xu et al., 2020), impeding their integration and further ecological applications. While some global multi-class land-cover products cover partial intertidal zones (Chen et al., 2014; Gong et al., 2019; Zhang et al., 2020), their classification algorithms are not designed for the coastal environment and mostly ignore a large part of intertidal areas. More recently, Mao et al. (2020) and Wang et al. (2020) mapped multi-class tidal wetlands at a national scale by applying a series of empirical thresholds on spectral indices or remotely-sensed inundation frequency, but their approaches depends highly on the selection of empirical thresholds which can vary with location and time of data acquisition (Zhao et al., 2020), thereby fails to offer a general solution that can be extended to other regions and periods to overcome those three challenges in remote sensing of tidal wetlands. At present, we still lack a robust, accurate and general tidal wetland classification framework to map multi-class tidal wetlands simultaneously. Instead of concentrating over a small area or a short period of time, the classification framework should be operational over a large geographical extent without dependence on prior knowledge such as tidal height at the image acquisition date, key phenological dates, manually delineated shoreline data, and empirical thresholds.

To overcome the above questions, this study proposed a novel classification algorithm, the Multi-class Tidal wetland Mapping by integrating Tide-level and Phenological features (MTWM-TP), to allow

large-scale mapping of TWC which includes mangroves, salt marshes, and unvegetated tidal flats simultaneously. To minimize the noise issue (such as residual clouds and spectral outliers) in the existing compositing techniques, MTWM-TP developed an automated approach to select scenes acquired at different tide levels and phenological stages to generate noise-free composite images representing tide-level and phenological information. We validated the role of integrating tide-level and phenological features in mapping tidal wetland composition by comparing with other classification methods and further tested the sensitivity of MTWM-TP to training sample size. Applying MTWM-TP to East Asia, we produced a sub-continental-scale tidal wetland composition map at 10-m resolution using S2 images on GEE and discussed its

performance compared with four existing tidal wetland products.

2. Materials and methods

2.1. Study area

The study area was confined to the coastal areas of East Asia (EA; mainland China and Korean Peninsula) (Fig. 1), which extend from 18.15°N in the humid tropics to 41.00°N in the semi-humid temperate zone. The eastern coast of Korean Peninsula was excluded because it is dominated by rocks rather than wetlands (Kim et al., 2020). The region has a temperate monsoon climate in the north and a tropical monsoon

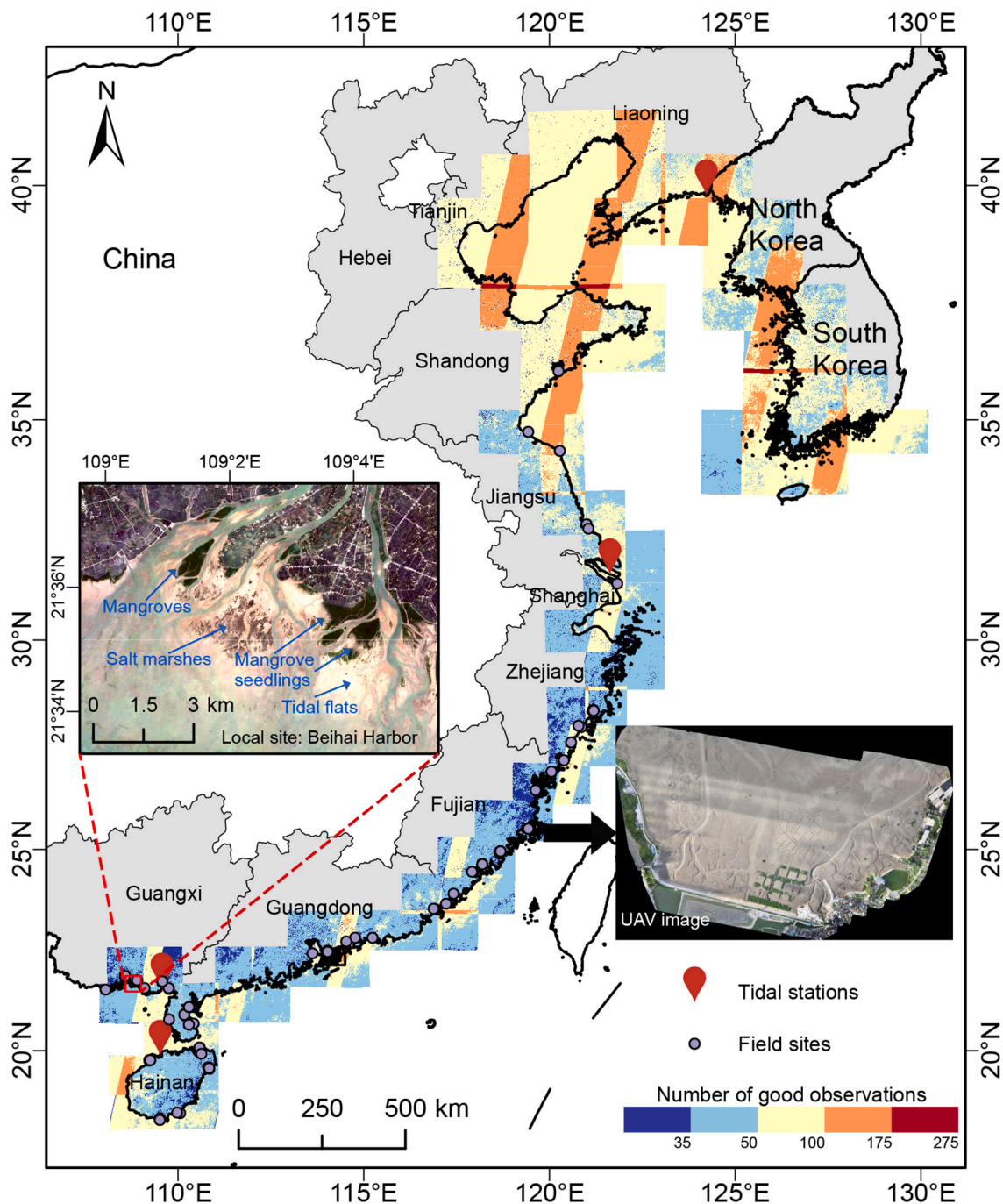


Fig. 1. Map of the study area, showing the location of field survey sites (Section 2.2.2) and tidal stations (Section 2.3.2). The red square indicates the location of BH. An example of UAV (unmanned aerial vehicle) orthomosaics obtained from our field survey in Luoyuan Bay, Fujian Province, China is also indicated. (For interpretation of the references to colour in this figure legend, the reader is referred to the web version of this article.)

climate in the south, with average annual temperatures ranging from 9 to 25 °C. Such a large area provides diverse climate and landscape settings to test the robustness and generality of our classification method.

We implemented the classification within 115 S2 tiles (100 × 100 km) (<https://sentinel.esa.int/web/sentinel/missions/sentinel-2/data-products>) intersecting with the coastline (<https://osmdata.openstreetmap.de/>). To minimize unnecessary processing, we limited our analysis to low-lying areas with surface elevation less than 25 m using the Advanced Land Observing Satellite World 3D data, a global digital surface model dataset with a vertical error of 4.1 m and a horizontal error of 5 m (Tadono et al., 2015), due to the low elevation of the coastal area. The 25 m cut-off preserves the tallest tidal wetlands in EA considering that the tallest tidal wetland (i.e., mangrove forest) stand of EA is 15.3 m with a 6.31 m error (Simard et al., 2019).

A local site located in the Beihai Harbor (BH) of Guangxi Zhuang Autonomous Region, China, was selected for demonstration purposes in this study. BH is an iconic mangrove-marsh ecotone that includes mature mangroves, mangrove seedlings, salt marshes, and unvegetated tidal flats simultaneously (Fig. 1). Such diverse landscape makes BH an desirable place to demonstrate the performances of our MTWM-TP algorithm in mapping TWC. BH experiences a southern subtropical monsoon climate with frequent cloud cover and rainy days (mean annual precipitation of 1600 mm), thus can serve as a specific site to examine the performance of our method in cloudy areas. Additionally, selection of BH was also motivated by the presence of existing field data and our familiarity with the site (Fig. 1).

2.2. Data sources

2.2.1. Sentinel-2 data

The Sentinel-2 mission comprises a constellation of two polar-orbiting satellites (Sentinel-2A and -2B), which were developed to observe global land surface dynamic with a short repetition time (5 days at the Equator after the launch of Sentinel-2B in March 2017). It offers publicly available multi-spectral images with 13 discrete spectral bands ranging from 440 to 2200 nm at a spatial resolution of 10–60 m. The relatively high spatio-temporal resolution increases the probability of obtaining cloud-free images during the low/high tide conditions and detecting small tidal wetland patches.

Our classification scheme was applied to time series of S2 Level-2A surface reflectance (SR) imagery for the year 2020 with six-month buffers prepended (18 months total) for capturing tidal variations and a full phenological cycle of vegetated wetlands. With more cloud and rain in the summer due to the monsoon climate, prepended six-month period ensures sufficient cloud-free growing season observations for EA. A total of 17,106 images taken from 1 Jun 2019 to 31 Dec 2020 were available, of which 6832 scenes almost completely covered by clouds (images with cloud cover greater than 70%) were filtered out to minimize cloud contamination according to Quality Assessment (QA) 60 bitmask band, resulting in a total of 10,274 S2 scenes across the study area for further analysis. While the QA band provides a tool for cloud and cloud shadow masking, the performance tends to be poor, with an average of 37.4% errors of omission (Coluzzi et al., 2018). We thus further masked out pixels covered by residual clouds and cloud shadows using the Fmask algorithm (Zhu et al., 2015) on GEE, obtaining an average of 63 cloud-free scenes per pixel with a standard deviation of 28 scenes (Fig. 1). Given that the Fmask was developed to run on top of atmosphere reflectance, we adapted the algorithm to perform directly on S2 SR images and observed reduced errors of omission for clouds and cloud shadows compared to the QA band and S2 Cloud Probability products of GEE (Fig. S1).

2.2.2. Training samples

Field surveys were carried out in 69 areas between May 2019 and October 2020 to collect training data and guide further sampling (Fig. 1). We acquired 758 sub-meter resolution images using a DJ

Phantom 4 pro Unmanned Aerial Vehicle (UAV) and the in-built RGB sensor during the low-tide condition as a reference to develop training samples and get visual experience on tidal wetlands. A total of 16,074 georeferenced polygons were collected as the training samples by referring to multiple sources, including existing global mangrove and tidal flat datasets (Bunting et al., 2018; Murray et al., 2019), S2 lowest tide composite images (see Section 2.3.3), high-resolution Google Earth images acquired during 2019–2020, and our UAV images. These training samples consist of five classes: “mangrove”, “salt marsh”, “tidal flat”, “permanent seawater” and “other” (Table 1), in which “other” represents terrestrial land-cover types, including inland vegetations, bare soils, and impervious surfaces. Note that the “other” category does not contain aquaculture ponds, as they have been represented by the “permanent seawater” category given that they are all water in terms of land cover, which allowed us to directly use “other” as “non-water” category when separate water from non-water area (see Section 2.3.4).

2.3. MTWM-TP classification algorithm

2.3.1. Overall classification framework

Based on the statistically significant spectral differences of tidal wetlands in different tide levels and phenological stages (Figs. S2–S3; see Supplementary Material for more details), we proposed a tidal wetland classification method that integrates tide-level and phenological features, namely, the Multi-class Tidal Wetland Mapping by integrating Tide-level and Phenological features (MTWM-TP). We separated the classification of tidal wetlands into three major components: mapping unvegetated tidal flats, classifying vegetated tidal wetlands (i.e., mangroves and salt marshes), and the post-processing step (Fig. 2).

In this study, tidal flats represent the mudflats and sandflats exposed during the low tide condition but submerged during the high tide condition (Table 1). Given this definition, seawater pixels at the highest tidal stage but mudflats or sandflats at the lowest tidal stage were detected as the tidal flats. The challenge then lies in obtaining the highest- and lowest-tide images for detecting the whole tidal flats. We thus developed a new method to automatically generate noise-free satellite-observable highest and lowest tide images and used Random Forest (RF) classifiers (Belgiu and Drăguț, 2016) to extract tidal flats. Note that because sun-synchronous satellites such as S2 can only observe a sub-portion of the full tidal range (Rogers et al., 2017; Sagar et al., 2017), the highest and lowest tides mentioned in this study mainly refer to the highest and lowest tides observed by S2 satellites (Jia et al., 2021) rather than extreme astronomical tide levels.

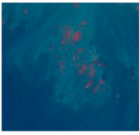
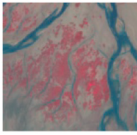
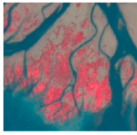
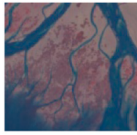
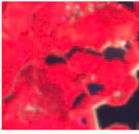
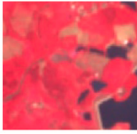
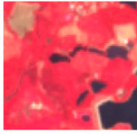
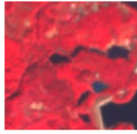
Mangroves and salt marshes mapped in this study refer to woody and herbaceous vegetation rooted in the intertidal environment, respectively (Kelleway et al., 2017). We inputted image composites that combined imagery corresponding to the high and low tides into the RF classifier to amplify spectral differences between vegetated tidal wetlands and inland vegetations. However, since both mangroves and salt marshes are affected by the tidal fluctuance, merely using tide-level features cannot be effective in distinguishing between these two tidal wetland types. Hence, we introduced phenological features into the classification scheme as the salt marshes have strong greenness seasonality but mangroves are evergreen. We proposed a new method to generate cloud-free green and senescence composite images, which were further combined with high- and low-tide images as features for the classification.

As the unvegetated tidal flats and vegetated tidal wetlands are mapped separately, a post-processing procedure is needed to integrate the individual results. In this step, we combined the results of two classification phases, applied several spatial processing techniques to reduce classification errors and uncertainties, and got the final classification map.

2.3.2. Generating noise-free lowest and highest tide images

To automatically identify low-tide and high-tide S2 scenes, we assumed a robust statistical relationship between spectral indices (SIs) of

Table 1
Definitions and image characteristics of land-cover types used in this study.

Class I	Class II	Description	Image characteristics (Standard false colour)			
			High tide	Low tide	Growing season	Dormant season
Tidal wetlands	Mangroves	Communities of shrubs or trees that grow in the intertidal area.				
	Salt marshes	Herbaceous vegetation rooted in the intertidal area.				
	Tidal flats	Mudflats and sandflats between highest and lowest tide levels.				
Other	Permanent seawater	The seawater below the lowest tide level.				
	Inland vegetation	Vegetation unaffected by tides, such as inland evergreen forests and grass.				
	Bare soils	Inland soil and sand without vegetation and building cover.				
	Impervious surfaces	Man-made hard areas like built-up areas, roads, ports, and seawalls.				

intertidal environment and actual tidal height. To verify this assumption, we selected four tidal gauging stations with different tidal types across EA from the website of China National Shipping Services (<https://www.cnss.com.cn/tide/>) (Fig. 1; Table 2) and recorded their tidal height at the acquisition time of cloud-free S2 scenes from 1 Jan 2020 to 31 Dec 2020. Then, for each S2 scene, we tested the relationship between actual tidal height and the average value of 8 spectral indices (SIs; Table S2) for tidal flat samples close to the corresponding tidal gauging station to determine the best proxy for tide level. Previous studies have reported that these indices may have positive or negative correlations with water level (Jia et al., 2021; Sagar et al., 2017; O’Connell et al., 2017; Chen et al., 2017), but it remains unclear which index has the best and stable performance in representing tide level.

The most robust performance was achieved by the Normalized Difference Vegetation Index (NDVI) and Normalized Difference Water Index (NDWI) according to their stable coefficient of determination (R^2) across all tidal gauging stations (Fig. 3; Fig. S4), suggesting that the average NDVI/NDWI of tidal flats in an S2 scene can represent the tidal height at the acquisition time of the scene. Specifically, the negative relationship between NDVI of tidal flats and tidal height indicates that the low-tide images can be automatically identified by filtering S2 scenes with the large NDVI value of tidal flat samples (Fig. 3). Therefore, we flagged each S2 scene with the spatially average NDVI value of tidal flat samples and then sorted them in descending order to select the

highly ranked scenes as the low-tide observations. The LETC images were generated by performing the maximum NDVI compositing method (using the “qualityMosaic” function in GEE; Holben, 1986) on these selected low-tide S2 scenes. Similarly, the positive relationship between NDWI of tidal flats and tidal height allowed us to obtain the HETC image by compositing images with highly ranked average NDWI of tidal flat samples (Fig. 3). Considering the tidal height may vary among estuaries across a tile extent so that a single average NDVI/NDWI value may failed to reflect actual tide level anywhere, we divided each tile into several subregions according to the estuaries within the tile (Bishop-Taylor et al., 2019), and carried out the above sorting steps for each subregion to obtain LETC/HETC images. Notably, although the minimum NDVI and the minimum NDWI can theoretically represent the highest and lowest tides, respectively (due to the low NDVI and high NDWI of the water), their performance is not as good as using the MaxVC in practice because small index values can also be caused by cloud contamination (Fig. S5). In the present study, the highly ranked images refer to the top 20% of images. This value could be dynamically adjusted according to the degree of cloud contamination. Larger or smaller the value will cause more noises or missing pixels in the final LETC/HETC image, respectively. Besides LETC and HETC images, we also produced median composites to represent noise-free low-tide and high-tide images. The LETC and HETC images were used to map tidal flats, and the noise-free low-tide and high-tide images were used to classify mangroves and salt

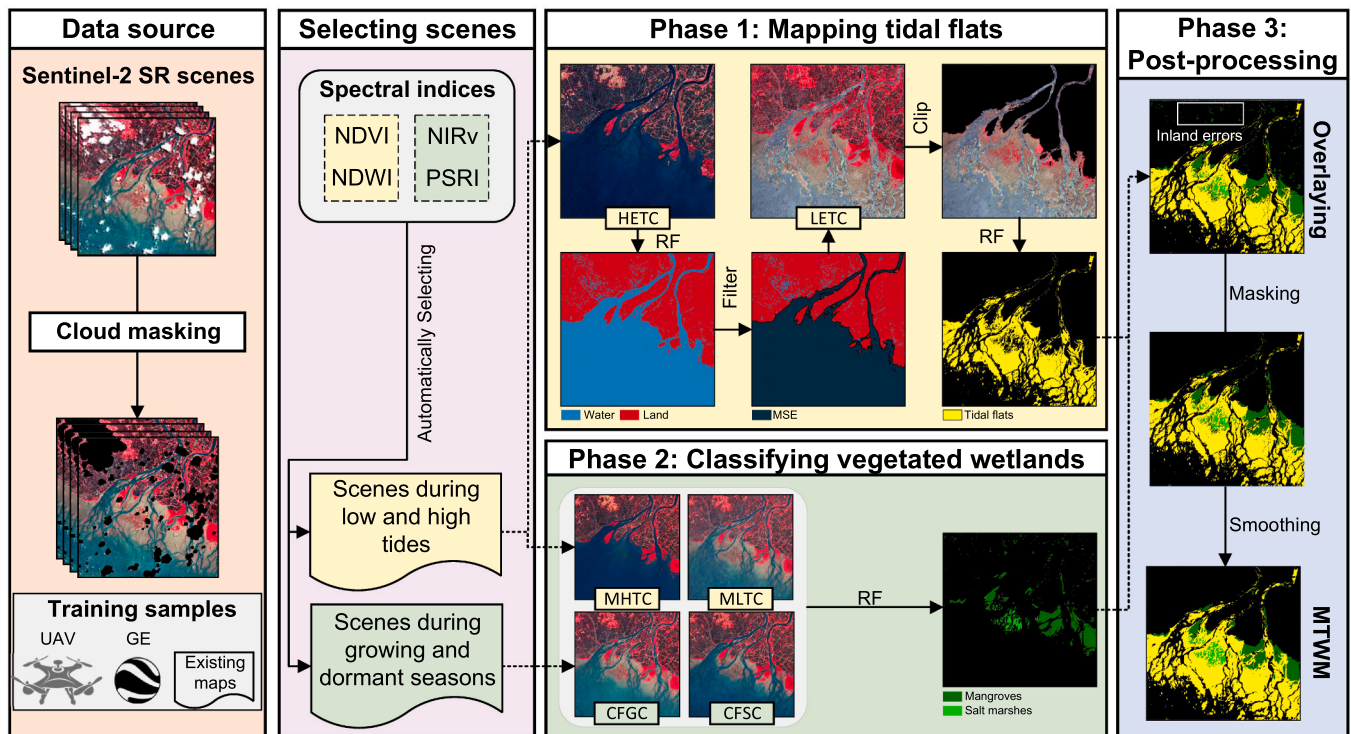


Fig. 2. Schematic flowchart of the proposed method MTWM-TP. MHTC: Median high-tide composite; MLTC: Median low-tide composite; HETC: Highest tide composite; LETC: Lowest tide composite; CFGC: Cloud-free green composite; CFSC: Cloud-free senescence composite; MSE: Maximum seawater extent; MTWM: Multi-class Tidal wetland Map. UAV: Unmanned aerial vehicle images; GE: Google Earth images. The images show the results of our method at BH. (For interpretation of the references to colour in this figure legend, the reader is referred to the web version of this article.)

Table 2
General information of tidal gauging stations used in this study.

Station	Location	Tidal type	Sentinel-2 overpass time (local time)	The number of cloud-free images
Dandong	39.81°N,124.14°E	Regular Semi-diurnal	10:36	59
Chongming	31.53°N,121.62°E	Irregular Semi-diurnal	10:49	34
Tieshan	21.58°N,109.56°E	Irregular diurnal	11:22	29
Xinying	19.90°N,109.50°E	Regular diurnal	11:22	20

marshes in the subsequent steps. An example performed at a cloudy tropical tidal station Xinying was shown in Fig. 4.

2.3.3. Generating green and senescence images

The traditional method of using phenological information in classification is to determine the dates of key phenological events. However, this method is limited in large-scale applications, as mentioned in Section 1. In this study, we switched the strategy from determining the key phenological dates to identifying images acquired during growing and dormant seasons. Since salt marshes are deciduous but mangroves are evergreen, the growing and dormant seasons mentioned in this study mainly refer to salt marshes.

We used Near-Infrared Reflectance of Vegetation (NIRv) (Table S2) to determine the growing-season images due to its high correlations with vegetation photosynthesis and superior performance in simulating vegetation phenology (Badgley et al., 2017). Higher NIRv indicates closer to the growing season. For a subregion, we flagged each S2 scene

with the average NIRv value of salt marsh samples and then sorted the images in descending order. The highly ranked images were labeled as the growing-season images and further composited to generate a cloud-free green composite (CFGC) image with the median composite method that is insensitive to outliers (Fig. 5a). The resulting composite contains the median observation for each band in each pixel. We used Plant Senescence Reflectance Index (PSRI) (Table S2) to determine senescence images for salt marshes (Fig. 5b) because higher PSRI represents closer to the end of the growing season (Tian et al., 2020). Similar to generating CFGC images, we generated cloud-free senescence composite (CFSC) images by compositing the highly ranked images with higher average PSRI of salt marsh samples. The composite images with different tide levels and phenological periods can be reproduced with the following GEE script: <https://code.earthengine.google.com/063d5c60e a567e892dca149a189176a5>.

2.3.4. Mapping of unvegetated tidal flats

According to the definition of tidal flats, the first step should be finding the maximum seawater extent (MSE) during the highest tide level. Since tidal flats are submerged by seawater at the high tide stage, we reassigned “permanent water” and “tidal flat” of training samples as “water”, and “other” training samples still as “other” for distinguishing water and land in HETC images (Fig. 2). Here we didn’t use “mangrove” and “salt marsh” samples in separating water from non-water area because some of them are submerged by seawater in the HETC images. This design does not cause exposed mangroves and salt marshes to be classified as water because they are more similar to terrestrial vegetation contained in the “other” samples rather than water in the spectral domain.

Random Forest (RF) was chosen to perform supervised classifications in this study due to its high accuracy and stability with less computational time than other classifiers (Pelletier et al., 2016). The number of decision trees (*Ntree*) in RF is an important parameter and was set to 200

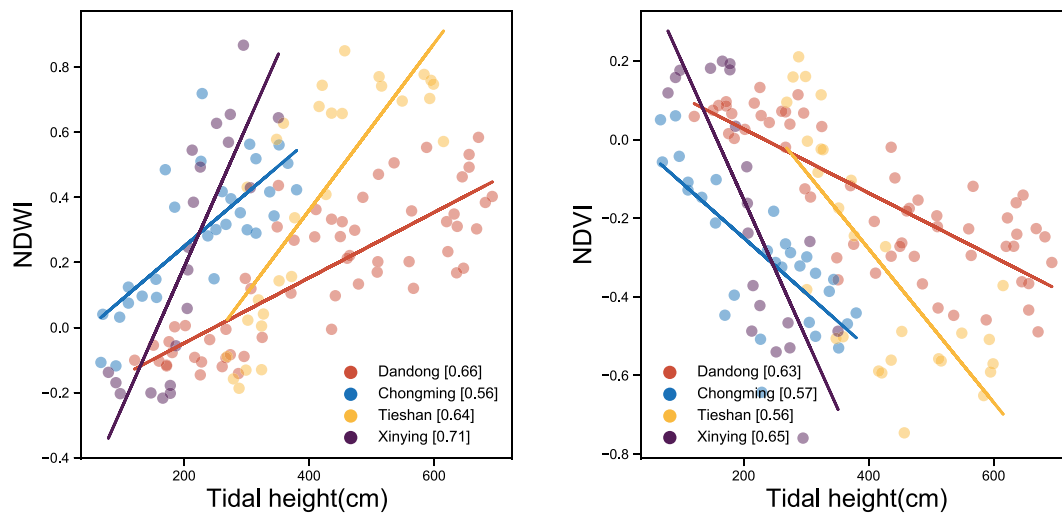


Fig. 3. Relationships between tidal height and two spectral indices. Each point represents an S2 observation. The number in brackets of the legend indicates R^2 . Note that $p < 0.05$ for all models. The tidal datum of Dandong, Chongming, Tieshan, and Xinying are 150, 214, 359, and 205 cm below the mean sea level, respectively.

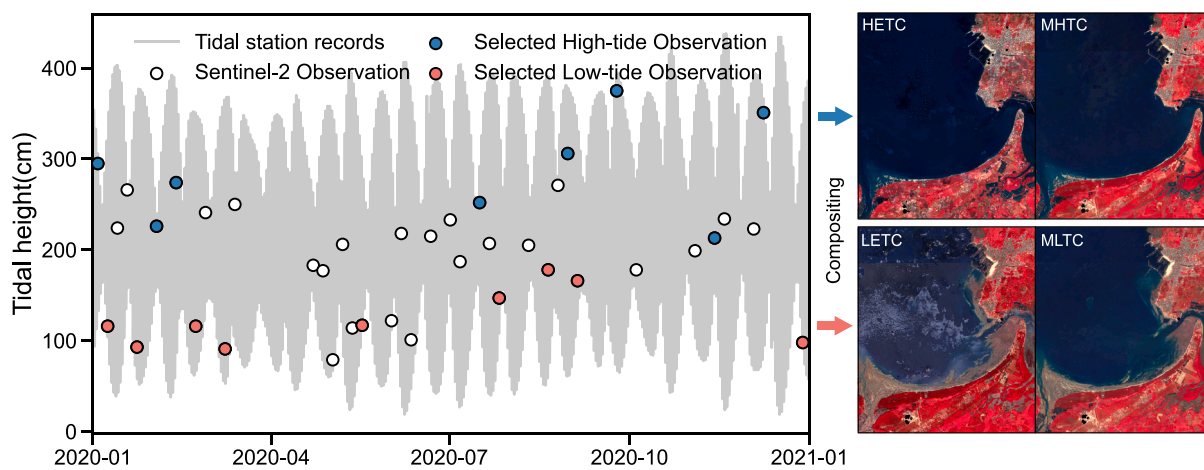


Fig. 4. Time series of tidal height in Xinying station and the derived composite images with different tide levels. The scatter points present Sentinel-2 observations. The blue points are the Sentinel-2 scenes with the top 20% NDWI of the tidal flat samples; the red points are the Sentinel-2 scenes with the top 20% NDVI of the tidal flat samples. The selected scenes were composited to generate low-tide and high-tide images by maximum spectral index and median composite methods. The tidal datum of Xinying is 205 cm below the mean sea level. (For interpretation of the references to colour in this figure legend, the reader is referred to the web version of this article.)

in this study by referring to previous works (Belgiu and Drăguț, 2016; Valderrama-Landeros et al., 2021). Our sensitivity test also indicates that 200 trees are large enough to ensure classification accuracy (Fig. S6). To avoid overfitting and enhance our classification's robustness, we trained ten independent RF classifiers for every classification of this study, each randomly selecting only 70% of total training samples with the same classifier parameters. The mode composite of the ten RF results was regarded as the most likely class for each pixel.

As an initial step, we classified each pixel in HETC images as “water” or “land” with classification features consisted of 12 spectral bands (i.e., all spectral bands in S2 SR image) and two spectral index bands (i.e., NDVI and NDWI). Lower resolution S2 spectral bands were resampled to 10-m pixel size using the nearest neighbor method. To exclude inland water bodies such as aquaculture ponds and lakes, we converted the “water” pixels to vector format and further determined the maximum seawater extent by selecting polygons that contain tidal flat samples (using the “filterBounds” function in GEE) (Fig. 2). Previous studies usually select the water polygon with the largest area as the MSE at this step (Jia et al., 2021; Lu and Wang, 2021). This approach would omit those seawater polygons isolated by cross-sea bridges, thereby

underestimate the actual MSE (see Fig. S7 for a specific example). Using the “containing tidal flat samples” criterion could take these isolated seawater polygons into account because we deliberately gave tidal flat samples to these seawater polygons when generating training samples. Additionally, we gave a “fake” tidal flat sample (It can be any actual land-cover types, but must be in the extent) for each omitted seawater polygons found when visually checking the classification results of water and land so that they can be selected according to the “containing tidal flat samples” criterion. Through this step, almost all inland water bodies would be masked out because they don't contain any tidal flats. The following procedure is the extraction process of tidal flats from the LETC images. We reassigned “permanent water”, “mangrove”, “salt marsh”, and “other” training samples as “other” samples and ensembled them with “tidal flat” samples into the RF classifier. We limited the classification within the intertidal environment by clipping the LETC images to the MSE layer to exclude spectrally similar terrestrial land-cover types like bare soils. Finally, we classified each pixel of the clipped LETC images to “tidal flat” or “other” using the mode composite of ten RF results. The classification was performed each three tiles along the coastline rather than at once for the entire study area considering

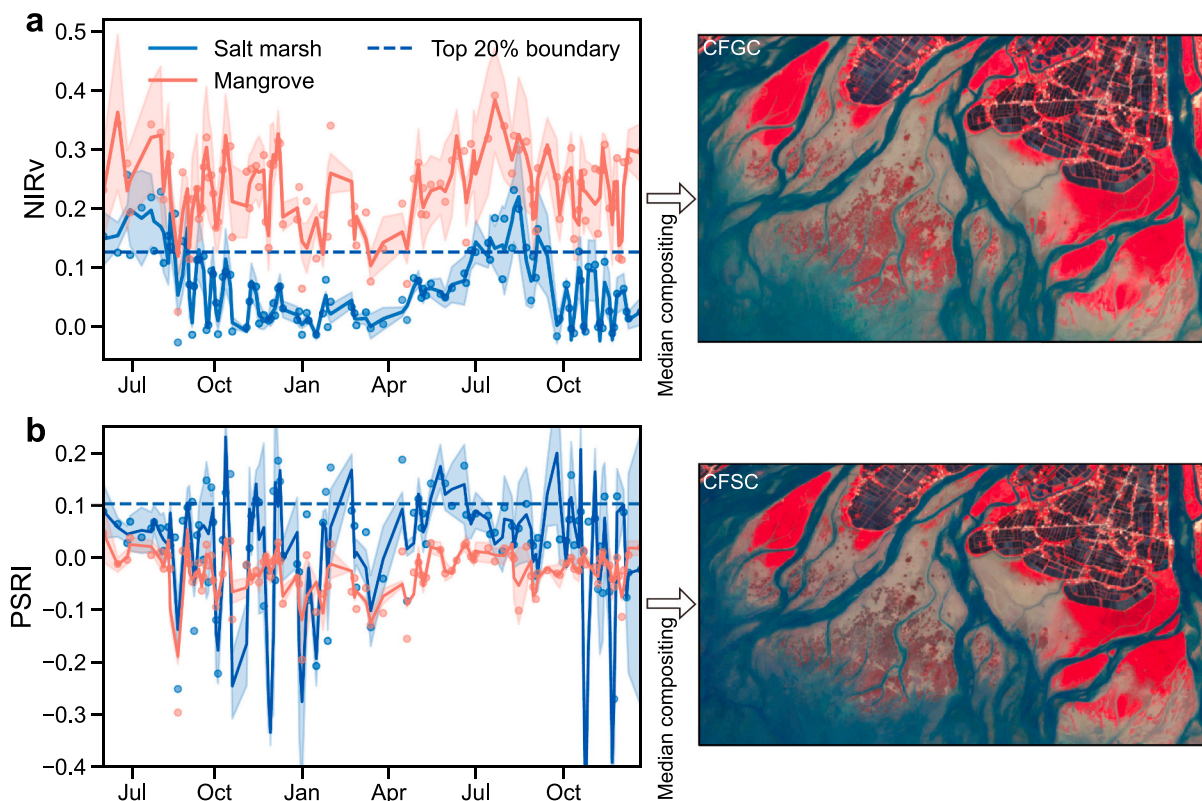


Fig. 5. Temporal profiles of NIRv and PSRI from mangroves and salt marshes in local site BH. The scatter points represent Sentinel-2 observations. Each profile is obtained by applying Savitzky-Golay smooth technology (Chen et al., 2004) for showing phenological dynamics. The shaded area refers to ± 1 standard deviation. Sentinel-2 observations with the top 20% average NIRv and PSRI of salt marsh samples were selected to generate CFGC and CFSC images.

that just one RF model cannot deal with the data variability arising from the landscape diversity for such a large area and to avoid exceeding the computation time and memory limits of GEE.

2.3.5. Classification of vegetated tidal wetlands

Both tide level and phenology were used in the classification scheme of vegetated tidal wetlands. We concatenated the median low-tide composite (MLTC), median high-tide composite (MHTC), CFGC, and CFSC images to create a 48 spectral bands image (12 bands each in the 4 composites), so that each pixel contains the spectral response observed at low tide, high tide, growing season, and dormant season. We re-assigned all training samples to three classes, including “mangrove”, “salt marsh” and “other”, and used ten independent RF classifiers to map mangroves and salt marshes on the concatenated image. Besides the spectral bands, we added the NIRv of the CFGC and CFSC images (hereafter NIRv_{green} and NIRv_{senescence}) and the NIRv difference (NIRv_{green}-NIRv_{senescence}) as classification features to account for the seasonal difference of greenness. The mode composite of the ten results (i.e., most frequent class for each pixel) was used as the final vegetated tidal wetland result.

2.3.6. Post-processing

By overlaying the tidal flat layer on top of the vegetated wetland map, we generated the Multi-class Tidal Wetland Map (MTWM). Since tidal flats and vegetated wetlands were mapped separately, some pixels were classified as both vegetation wetlands and tidal flats. These pixels are mainly distributed around the edges between tidal flats and vegetated wetlands, suggesting that the spectral mixture caused this issue. As a “hard classification” study, these pixels can only have one label. In such a case, we corrected these pixels from mangroves or salt marshes to tidal flats because they have a higher probability of being tidal flats than vegetated wetlands supported by their NDVI distribution probability

(Fig. S8). Experiments later in this study (Fig. 10b) also show that the method of mapping tidal flat has higher accuracy than classifying vegetated wetlands across all training sample sizes, suggesting these pixels are more likely tidal flats. Although we used the tide level features to distinguish between inland land-cover types and tidal wetlands, some inland errors still exist due to RF classification errors. As such, we further removed inland error to reduce the commission errors by excluding tidal wetland polygons not intersect with the 500-m buffer of MSE generated in phase 1. Note that we used the “intersect” rather than “clip” criterion in this procedure, which means any tidal wetland patch that intersects with the buffer of MSE would be retained entirely. Since the MSE contains rivers connected to the ocean (see Fig. 2), the 500-m buffer radius is wide enough to account for all riverine tidal wetlands based on the “intersect” criterion. Furthermore, to add a degree of robustness and remove erroneous edge pixels between different land-cover types within the MTWM, pixels that were not surrounded by their same land-cover types were converted to the most distributed type nearby using a majority filter with a 5×5 moving window (McCarthy et al., 2018).

2.4. Accuracy assessment

As for the validation samples, a stratified random sampling scheme was adopted to avoid arbitrariness and bias in the accuracy assessment (Stehman and Foody, 2019). We calculated that 2746 samples would be sufficient for the validation using a commonly used sample size formula (Stehman and Foody, 2019), as shown below:

$$n = \frac{z^2 p(1-p)}{d^2} \quad (1)$$

where $z = 1.96$ for a 95% confidence interval, d is the half-width of the desired confidence interval ($d = 0.025$ in this study), p is the anticipated

proportion of correct classifications for a particular class (we used the area proportion as the p for each wetland class). For the “other” class, we set p as 0.5 for deriving a large enough value (because at this value, the term $p(1-p)$ is maximized) due to the lack of knowledge on the anticipated proportion of the correct “other” class.

Considering the relatively rare mangrove in the study area, we increased mangrove test samples from 90 to 200 by referring to Olofsson et al. (2014), who suggests the allocation of test samples could be shifted slightly away from proportional allocation by giving more test samples to the rare class. As a result, we generated a validation set consisting of 2856 random points (at 10-m scale) within the tidal wetland extent and within a 1-km buffer from the MSE (Fig. S9). These points were assigned to one of 4 classes: “mangrove”, “salt marsh”, “tidal flat”, and “other”, with a direct reference to 1) LETC and CFSC images, 2) Google Earth images, and 3) UAV images if the validation points located in our survey areas.

Four metrics were used in validation processes: User's Accuracy (UA), Producer's Accuracy (PA), Overall Accuracy (OA), and F1 score. UA quantifies the proportion of a tidal wetland class in the satellite-derived map consistent with the reference data and therefore measures commission errors. PA quantifies the probability of a tidal wetland class on the ground correctly classified by the satellite-derived map, measuring omission errors. OA quantifies the fraction of all correctly classified validation points. F1 score is the harmonic mean of PA and UA and could be a tradeoff metric to quantify both omission and commission errors for each class (Bargiel, 2017).

For comparison with our MTWM, four publicly available tidal wetland maps covering our study area were chosen, including 1) global tidal flat data in 2014–2016 produced by Murray et al. (2019) (Murray_TF), 2) two mangrove maps in 2015 published by Chen et al. (2017) and Hu et al. (2018) (Chen_MG and Hu_MG, respectively), and 3) wetland layer in 2020 selected from the latest global land cover map developed by the National Geomatics Centre of China (Globe30) (Chen et al., 2014). We compared the performance of these datasets on mapping tidal wetlands by using the same validation samples with the corresponding true-value label. Although the period of these datasets differs, a quantitative comparison still serves as a reference for assessing data quality, given that the time difference is less than or equal to only five years.

2.5. Comparing with other methods

To examine the role of integrating tide-level and phenological features in vegetated tidal wetland classification, we run four classifications at BH with the same training samples and RF parameters but different input classification features: 1) the spectral bands of the median composite image, which serves as a reference without using either tide level or phenology information, 2) the spectral bands of MHTC and MLTC, which represents the using of only tide-level feature, 3) the spectral bands of CFGC and CFSC, which represents the using of only phenological feature, and 4) the spectral bands of MHTC, MLTC, CFGC and CFSC, which serves as both using tide-level and phenological features. We also tested whether there would be a difference in classifications of using composite and original images. For this, we performed the classification on the concatenated image of four original S2 images with different tide-level and phenological stages (Table S1).

We developed a modified k -fold cross-validation approach to rigorously evaluate the performance of different classification strategies considering that the traditional k -fold cross-validation method has strongly biased accuracy estimates when the sample size is small (Rodriguez et al., 2009). Firstly, all samples were randomly divided into initial training and testing sets with a 7:3 ratio. These training samples were then randomly divided into k partitions (k equals 5 in this study), each partition combined with the initial testing set was further used once as the actual testing set to evaluate the classification result derived from the remaining $k-1$ partitions (i.e., actual training set). This process

was repeated 20 times so that there are 100 (20 times k , where k equals 5) independent evaluations to provide a robust estimate of classification performance. Such a strategy can guarantee the independence and randomness of training and testing samples, and increase the size of the testing set with limited total samples. One-way analysis of variance (ANOVA) and Tukey honestly significant difference (HSD) post-hoc test were finally performed to determine statistically significant differences among classification methods.

2.6. Testing the influence of training sample size

We performed the MTWM-TP algorithm on BH using varying sizes of the training pixels from 10 to 150 for each land-cover class with a step of 10 to examine the effects of the sample size on the classification performance. We firstly created a sample pool containing 200 pixels for each class, 30% of which were then randomly selected as test sets. Actual training samples were randomly collected from the remaining samples with an equal allocation norm. For each sample size, we performed the classification 100 times to reduce stochastic error. The OA and the F1 score for each wetland type were finally evaluated to assess the performance.

3. Results

3.1. Accuracy assessment of MTWM

The tidal wetland composition of EA was accurately mapped with user's and producer's accuracies exceeding 94% for all classified wetland types and with a high overall accuracy of 97.02% (Table 3). All F1 scores for the three tidal wetland classes were higher than 0.95 with less than 0.2 differences, suggesting a good balance between commission and omission errors and consistent performance among tidal wetland types.

Compared to other tidal wetland maps, MTWM has considerable advantages in classification accuracy (Table 4). Both Chen_MG and Hu_MG achieve high UA at about 93% with significantly lower PA, indicating more omission errors than commission errors. Murray_TF has much lower accuracy in mapping tidal flats than MTWM, with 68.50% UA and 78.50% PA. This means that Murray_TF omits some tidal flats and also incorrectly contains a lot of non-tidal flats areas. Globe30 has a high UA but the lowest PA in mapping tidal wetlands, implying a significant omission error. The relatively low F1 scores indicate that these existing products are limited in the balance of omission and commission errors.

3.2. Spatial pattern of tidal wetlands in East Asia

Tidal wetlands in EA in 2020 covered an area of 1,308,241 ha, calculated using an Albers conic equal-area projection (Fig. 6; Table 5). Our estimate indicates that the area varies greatly among different wetland types at the sub-continental scale. Unvegetated tidal flats covered the majority portion and were widely distributed along most coastlines, accounting for 89.12% of total intertidal zones (1,165,888 ha), while salt marshes and mangroves were less prevalent. About 70% of tidal flats occurred in China (820,031 ha), primarily in estuaries and deltas with large tidal ranges and high sediment inflows (Figs. 6-7). There was also a large extent of tidal flats on the Korean Peninsula, with an area of about 42% of China's tidal flats. At the province level, Jiangsu had the greatest extent of China's tidal flats (251,859 ha), followed by Shandong (118,715 ha) and Fujian provinces (89,679 ha). Vegetated tidal wetlands covered an area of 142,350 ha, of which salt marshes accounted for the majority and mangroves only 13.70%. All mangroves in the study area occurred in southern China, with about 80% in Guangdong and Guangxi provinces (Table 5). Salt marshes were observed across the entire extent of East Asia except for Hainan island, indicating broader geographical distribution than mangroves. As the mouth of the Yangtze River, the largest river in Asia (Fig. 7e), Shanghai

Table 3
Error matrix of validation samples for tidal wetland classification.

Classes	Reference				Total	UA	F1 score
	Mangroves	Salt marshes	Tidal flats	Other			
Mangroves	188	0	6	6	200	94.00%	0.96
Salt marshes	1	496	17	9	523	94.84%	0.97
Tidal flats	0	2	574	20	596	96.31%	0.95
Other	2	1	21	1513	1537	98.44%	0.98
Total	191	499	618	1548	2856		
PA	98.43%	99.40%	92.88%	97.74%			
OA							97.02%

Table 4
Classification accuracy of existing tidal wetland products.

	Chen_MG (mangroves)	Hu_MG (mangroves)	Murray_TF (Tidal Flats)	Globe30 (Tidal wetlands)
UA	93.24%	93.42%	68.50%	93.87%
PA	84.15%	86.59%	78.50%	48.05%
F1 Score	0.89	0.90	0.73	0.64

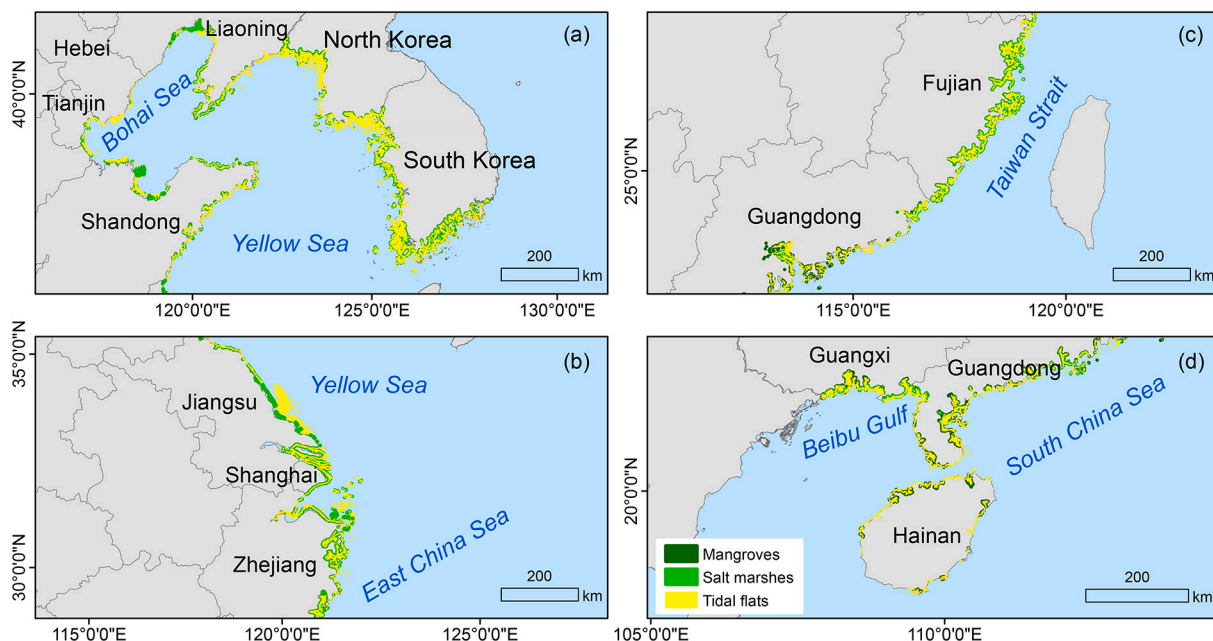


Fig. 6. Distribution of tidal wetlands along the coasts of East Asia in 2020. Four panels show the distribution of tidal wetlands in (a) the Bohai Sea and the northern Yellow Sea, (b) the southern Yellow Sea and the East China Sea, (c) the Taiwan Strait and the northern South China Sea, and (d) the South China Sea and the Beibu Gulf. (For interpretation of the references to colour in this figure legend, the reader is referred to the web version of this article.)

Table 5
Regional areas and percentages of tidal wetlands.

	Mangroves (ha)		Salt marshes (ha)		Tidal flats (ha)		Tidal wetlands (ha)
Korean Peninsula	0	0%	12,991.3	3.62%	345,856.5	96.38%	358,847.8
China	19,510.5	2.06%	109,850.7	11.57%	820,031.8	86.37%	949,393.0
Liaoning	0	0%	3319.3	3.90%	81,710.8	96.10%	85,030.1
Hebei	0	0%	162.0	0.44%	36,305.3	99.56%	36,467.3
Tianjin	0	0%	87.7	2.15%	3997.6	97.85%	4085.3
Shandong	0	0%	20,759.8	14.88%	118,714.8	85.12%	139,474.6
Jiangsu	0	0%	22,373.6	8.16%	251,858.8	91.84%	274,232.4
Shanghai	0	0%	31,449.1	49.80%	31,707.1	50.20%	63,156.2
Zhejiang	30.8	0.03%	20,782.0	20.97%	78,302.6	79.00%	99,115.4
Fujian	738.3	0.75%	8643.4	8.73%	89,679.2	90.53%	99,060.9
Guangdong	8854.4	12.13%	418.0	0.57%	63,716.5	87.30%	72,988.9
Guangxi	6828.9	12.12%	1855.8	3.29%	47,665.4	84.59%	56,350.1
Hainan	3058.1	15.74%	0	0.00%	16,373.7	84.26%	19,431.8
Total	19,510.5	1.49%	122,842.0	9.39%	1,165,888.3	89.12%	1,308,240.8

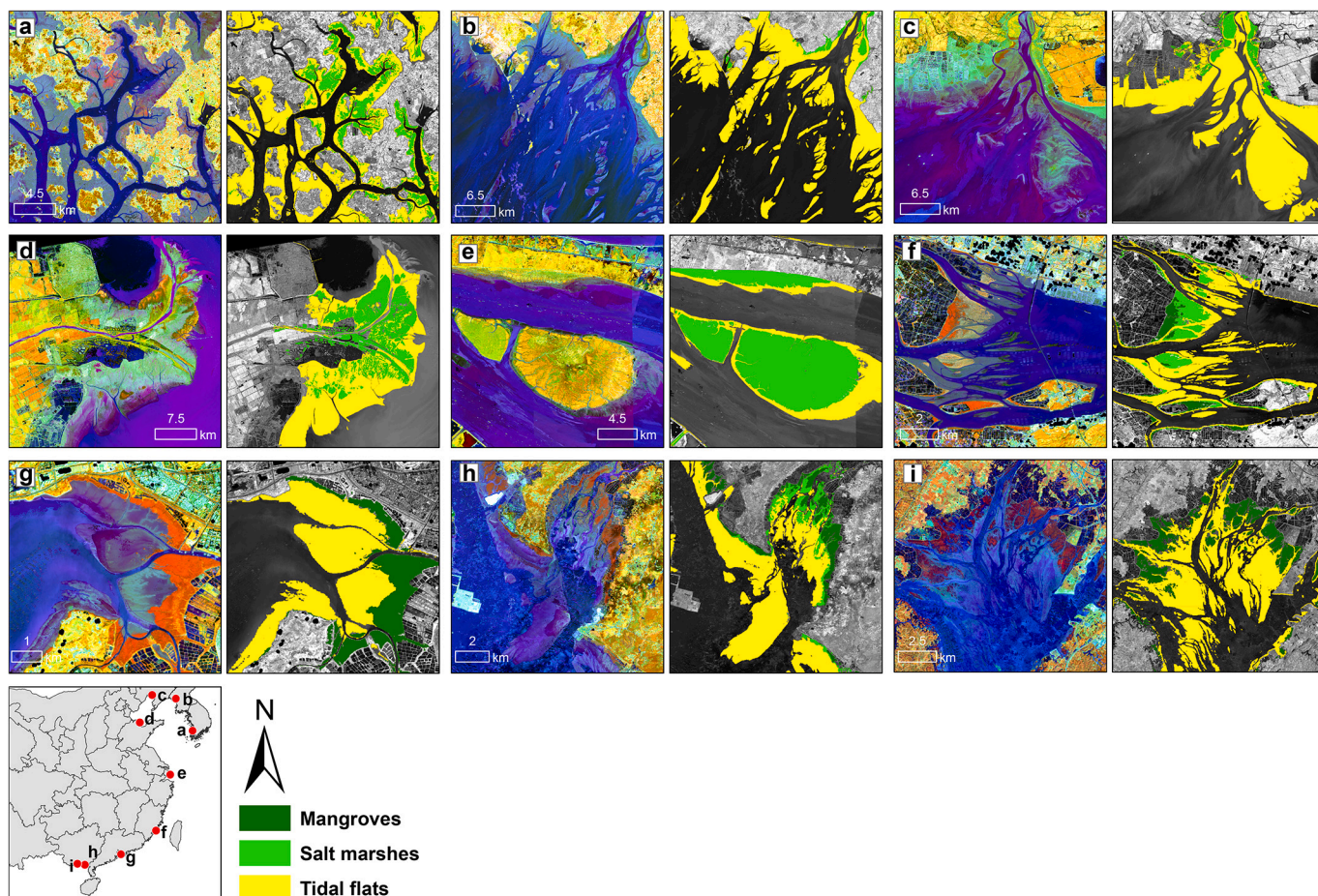


Fig. 7. Tidal wetland maps overlaid on the LETC images (R: band8, G: band11, B: band4) for nine locations: (a) Sinan County in South Korea; (b) Estuary of Taeryong River in North Korea; (c) Estuary of Liao River in Liaoning, China; (d) Yellow River Delta in Shandong, China; (e) Jiuduansha in Shanghai, China; (f) Estuary of Jiulong River in Fujian, China; (g) Shenzhen Bay in Guangdong, China; (h) Dandou Sea in Guangxi, China; (i) Maowei Sea in Guangxi, China. (For interpretation of the references to colour in this figure legend, the reader is referred to the web version of this article.)

had the greatest extent of salt marshes, accounting for 29% of China's salt marshes, almost double the area of the salt marshes on the Korean Peninsula. More than 85% of China's salt marshes occurred in warm temperate or northern subtropical regions such as Shanghai, Jiangsu, Shandong, and Zhejiang. In geographically tropical areas (south of Tropic of Cancer), salt marshes were replaced by mangroves in the

intertidal environment (Fig. 7g and i), such as in Guangdong, Guangxi, and Hainan (Table 5).

3.3. Comparison of different classification methods

We found statistically significant variation in accuracy among

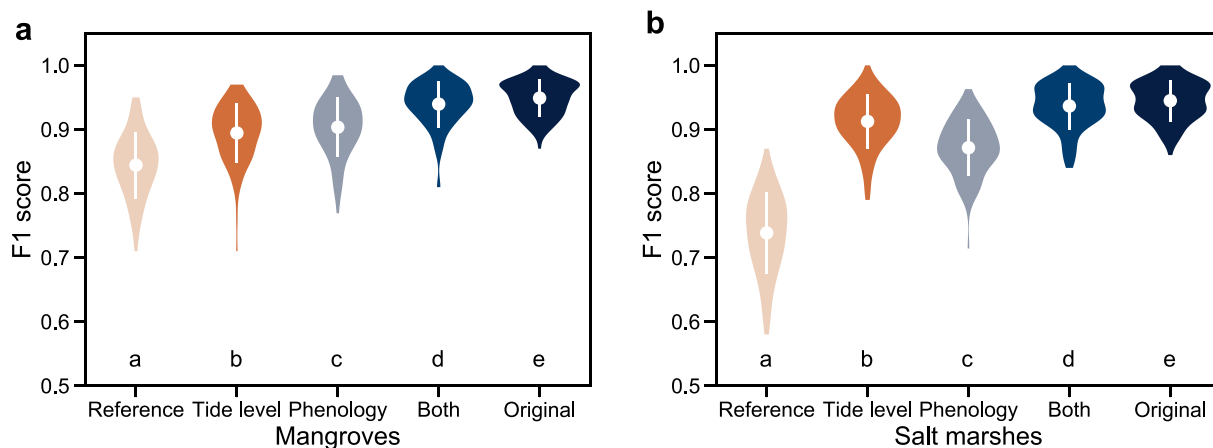


Fig. 8. Classification accuracies of five classification strategies for mapping (a) mangroves and (b) salt marshes. The violins show the probability density distribution of the accuracy. White points within the violins mark the median. Error bar within the violins represents ± 1 standard deviation of the mean. Different letters indicate significant differences between classification strategies (one-way ANOVA, Tukey HSD post-hoc test, $p < 0.05$).

classification methods in mapping both mangroves ($F = 102.85$, $p < 0.001$) and salt marshes ($F = 380.25$, $p < 0.001$). Of the features investigated, classification without tide-level or phenological features indicated the poorest performance in mapping both mangroves and salt marshes revealed by the Tukey HSD post-hoc test (Fig. 8). It failed to properly distinguish tidal wetlands from terrestrial landscape, especially for salt marshes (Fig. 9b1). Introducing tide level feature in the classification significantly improved the accuracy by separating tidal wetlands from inland areas, but some confusion between mangroves and salt marshes remained, which mainly occurred in the mangrove seedlings and mangrove edges (Fig. 9b2). The use of phenological features reduced the proportion of mangrove seedlings classified as salt marshes, but the inland errors reappeared (Fig. 9b3). Compared to only using tide level or phenological features, integrating tide-level and phenological features had a statistically significant accuracy improvement of 0.05–0.07 (F1 score) in mapping mangroves and salt marshes (Fig. 8; Fig. 9b4). In the case of using both tide-level and phenological features, the original S2 image just achieved a slightly higher F1 score (~ 0.01) in mapping both mangrove forests and salt marshes than composite images (Fig. 8; Fig. 9c), suggesting that composite images could achieve comparable accuracy with original high-quality images.

3.4. Sensitivity to training sample size

With the increase of training samples, the OA and F1 score of each class increased at first and then saturated (Fig. 10). The standard deviation of accuracy significantly decreased with the increases of sample size, suggesting that using a large sample size could achieve stable performance. Even with a very limited sample size (10 training pixels for each class), MTWM-TP still performed well, with OA of 84% and F1 scores over 0.8 for each tidal wetland. Tidal flats had the highest F1 score across all sample sizes, especially when the sample size was limited. The accuracy of each wetland class got closer as the sample size increases.

4. Discussion

This study presents a novel classification algorithm for mapping TWC based on multi-spectral time series, which uses spectral differences of tidal wetlands between high- and low-tide levels to separate them from adjoining terrestrial landscapes and uses spectral characteristics of growing and dormant seasons to distinguish mangroves and salt marshes. The derived 10-m resolution map of TWC for EA proves its great potential for large-scale applications.

4.1. Composite images with different tide levels and phenological stages

High-quality image composites are critical for a variety of applications (Roberts et al., 2017). For remote sensing of coastal environment and vegetation, a major challenge lies in generating noise-free composite images with different tide levels and phenological stages. Instead of compositing all the available images, as performed by previous studies (Jia et al., 2021; Murray et al., 2019; Zhao et al., 2020), this study developed a new method compositing automatically identified images acquired during high- and low-tide levels and during growing and dormant seasons (see Section 2.3.2 and 2.3.3).

Compositing the entire time-series stack of optical imagery without any filter is particularly sensitive to clouds or other noise. Although commonly used optical imagery (e.g., MODIS, Landsat, and Sentinel-2) mostly provides cloud mask bands, some thin clouds on coastal areas remain due to their poor performance and variations among data sources. For instance, the S2 cloud mask has many cloud detection omissions due to the lack of a thermal infrared band, introducing noise into S2 composites (Coluzzi et al., 2018). Even for cloud cover free Synthetic Aperture Radar data, compositing all available images would still reduce the quality of the composited image due to accumulated speckle noise (Lopez-Martinez and Fabregas, 2003), which affects the classification results to a certain extent. To alleviate the influence of image noise, we performed the MaxVC algorithm on the selected low-tide/high-tide images to obtain the noise-free LETC/HETC images. Using the selected image instead of all images reduces the probability of

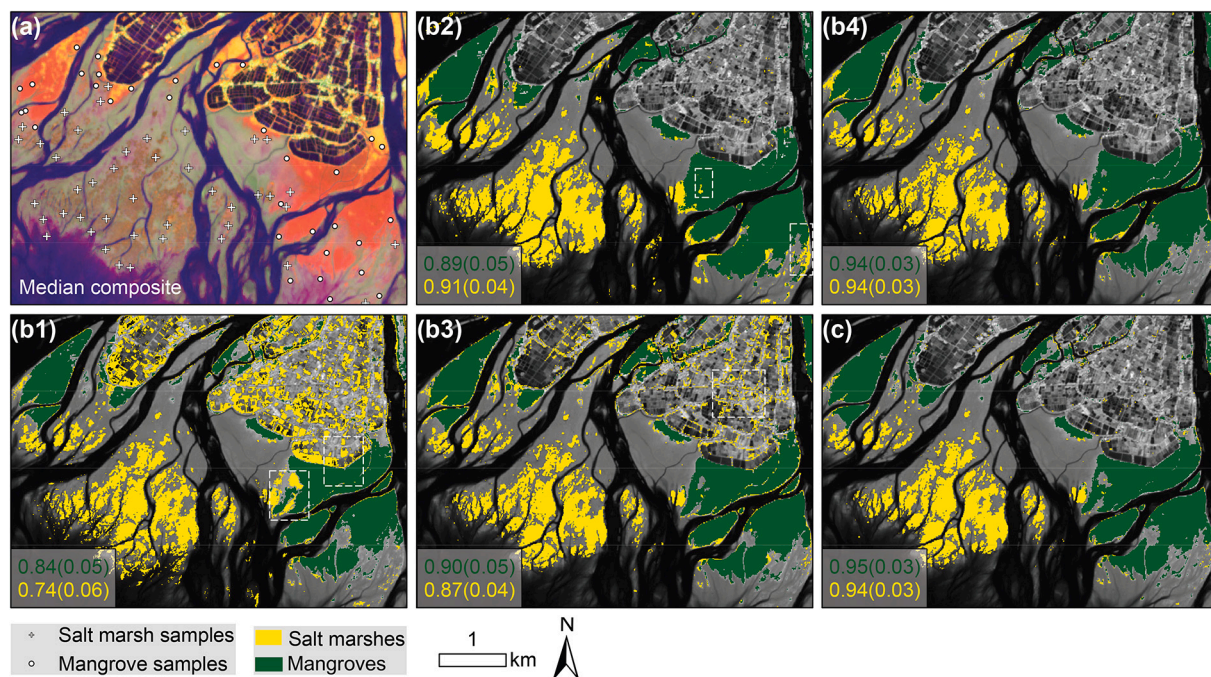


Fig. 9. Classification results for BH with the same training samples overlaid on (a) the median composite image (R: band8, G: band11, B: band4) by using (b1) usual spectral bands without considering either tide level or phenology, (b2) tide level, (b3) phenology, (b4) both tide level and phenology from composite image, and (c) both tide level and phenology from original S2 images (see Table S1 for the specific images). The number in brackets of legend indicates the standard deviation of accuracy for each type determined using the modified 5-fold cross-validation. Dashed boxes mark some obvious classification errors.

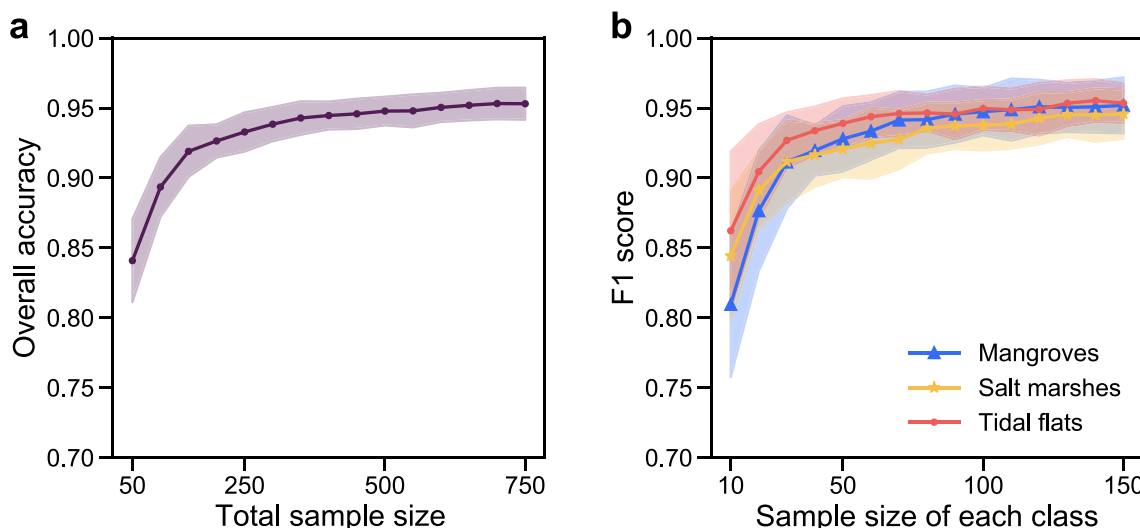


Fig. 10. Sensitivity of the accuracy to training pixel size. (a) Variations in OA; (b) Variations in F1 score of three tidal wetland classes. The shaded areas refer to ±1 standard deviation.

image noise occurrence while ensuring the capture of the fully tidal flats, as shown in Fig. 11. The high quality of composite image benefits the classification and help achieve similar performance compared with classification on the clear-sky original images, which are almost unavailable in practice (Figs. 8–9).

Our proposed method of generating CFGC and CFSC images is independent of investigating the exact dates of growing and dormant seasons. We used the median of VIs instead of the maximum value to composite the time-series stack of images for generating the CFGC and CFSC images because the maximum value reduces the inter-class greenness difference. For example, dense salt marshes may have similar greenness as mangrove seedlings during their peak growth period. In contrast, the median value (calculated over time) can capture the difference in greenness between deciduous marshes and evergreen mangroves, whatever the canopy density. We have not used the phenological parameters (such as the start of season (SOS) and end of season) as classification variables to classify wetland vegetations, as performed by Sun et al. (2021), because several factors need to be

considered. First, determining phenological parameters requires enough cloud-free and low-tide observations to reconstruct the full life cycle of vegetation greenness, limiting its application in cloudy areas such as tropical intertidal zones (Zeng et al., 2020). Besides, extracting phenological parameters is highly sensitive to curve fitting methods. Previous studies have reported that the difference in SOS derived by different curve fitting methods can exceed 60 days (White et al., 2009). Thus, any errors in phenological parameter extracting would introduce uncertainty into the final classification results. Furthermore, extracting phenological parameters for evergreen vegetation (Caparros-Santiago et al., 2021) such as mangroves is expected to be invalid due to insignificant greenness seasonality. In contrast, our method using the spectral bands during different phenological periods to amplify spectral separation between evergreen mangroves and deciduous salt marshes, which is robust to missing data and eliminates uncertainty caused by curve fitting methods.

Another major flaw of phenological parameter methods is their inability in large-scale applications. Since phenological parameters

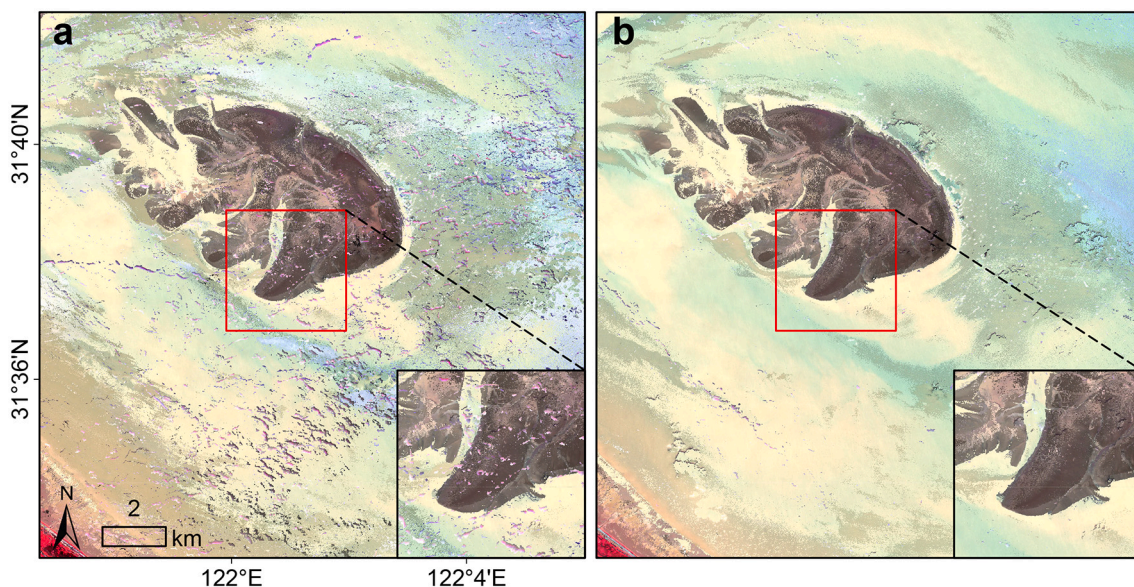


Fig. 11. Comparison of LETC images generated using (a) all S2 observations and (b) automatically selected low-tide observations with the same cloud masking procedure (Fmask algorithm) at Yangtze River Estuary.

(such as SOS) vary with climate and latitude (Caparros-Santiago et al., 2021), their use in classification can be highly uncertain and requires a comprehensive sample set to take such phenology differences into account. To examine the generality of our phenology method, we conducted an additional experiment that compared the key phenology dates and spectral characteristics during growing seasons for salt marshes in two local sites with distinctly different climates and latitudes (Fig. 9b). We observed that the growing season of salt marshes in the high-latitude Taeryong River Estuary was delayed by 15 to 20 days compared to low-latitude BH in 2020 (Fig. 12a). In contrast, the spectral characteristics of salt marshes during growing seasons in these two sites were similar, suggesting the same vegetation type at different places have similar spectral characteristics during their respective phenological stages. Consequently, using the spectral characteristics of different phenological stages instead of specific phenology dates has great potential in large-scale mapping or simultaneous classification for two places with different latitudes or climates.

4.2. Advantages of MTWM compared to existing products

Visual comparisons between MTWM and existing tidal wetland products are shown in Fig. 13. The difference in the total area of tidal flats between MTWM and Murray_TF was more than 360,000 ha (Table 6). Such a huge difference is mainly caused by different considerations of tide-level information. Murray_TF used quantile composites of water indices as predictor variables in the RF classifier to account for tidal dynamics for each pixel. However, as aquaculture ponds and some inland lakes have dry periods (Pekel et al., 2016), the underlying soils would be exposed and thus be incorrectly detected as tidal flats by the quantile composite of the water indices. Additionally, large areas of salt marshes were misclassified as tidal flats in Murray_TF due to their low greenness and similar inundation frequency to tidal flats. Moreover, since the lowest tide image was not used, a lot of lower tidal flats were not captured in Murray_TF (Fig. 13a). In contrast, inland pixels were masked out in MTWM by using the MSE, and all lower tidal flats observed by satellites were captured using 10-times independent RF classification on LETC images.

The mangrove area derived from MTWM is lower than that of Chen_MG but higher than that of Hu_MG (Table 6). Both Chen_MG and HU_MG represent the year of 2015 while the MTWM product is for 2020, so some differences in the area were expected. However, the visual comparison shows that these differences are unlikely to be attributed to actual changes but rather due to classification errors in the products

(Fig. 13b). Mangroves in Chen_MG were mapped by identifying evergreen pixels with a dense canopy and tidal inundation. This approach could detect periodically flooded low-stand mangroves, as these mangroves are unique evergreen woody vegetation in the intertidal environment which would be submerged by high tide. However, for high-stand mangroves that are not fully submerged by tides, their similar greenness frequencies and canopy cover with inland evergreen cause significant omission errors (Table 4). For example, a part of high-stand fringing mangroves that occur along the upper tidal channel were omitted in Chen_MG (Fig. 13b). In contrast, MTWM could detect these high-stand mangroves by combining spectral characteristics under different tide levels instead of directly recognizing the submerged state of mangrove canopies. Hu_MG used the quantile composites of spectral reflectance to separate mangroves from other vegetation types such as cropland and terrestrial forests. We observed obvious errors of omission for high-stand mangroves in Hu_MG (Fig. 13b). This is likely due to the similar spectral quantile between mangroves and other evergreen forest types. Quantile composites, used in Hu_MG, cannot detect the phenological difference between similar landscape such as mangroves and inland evergreen forests because these landscapes have similar SI quantiles (e.g., maximum value and median value) over a year, but the date of reaching the specific greenness (e.g., the peak) is different. The quantile composite method cannot reflect this temporal information and therefore confuses phenologically similar vegetation types. In this regard, phenological information used in our method was based on automatically selected images of growing and dormant seasons. It also should be noted that both Chen_MG and Hu_MG were mapped using Landsat imagery with 30-m spatial resolution, which is too coarse to capture the detailed feature of mangrove forests, such as tidal channels and canopy gaps (Fig. 13b).

Larger tidal wetland areas were detected by our map than Globe30 (Table 6). The difference is primarily due to methodological approaches such as the use of LETC images. Although including the wetland layer, Globe30 has not subdivided the wetland category into specific types such as mangroves, salt marshes and tidal flats (Fig. 13c). Global land-cover products tend to lack specific design for intertidal environments and thus limit to detection of large areas of submerged salt marshes, low-stand mangroves and tidal flats. By overlaying Chen_MG and Murray_TF, we observed that some pixels were classified as multiple categories, illustrating errors presented in each map would be compounded in the final multi-class maps if overlaying multi-source wetland datasets. As such, mapping tidal wetland composition is necessary for practical applications.

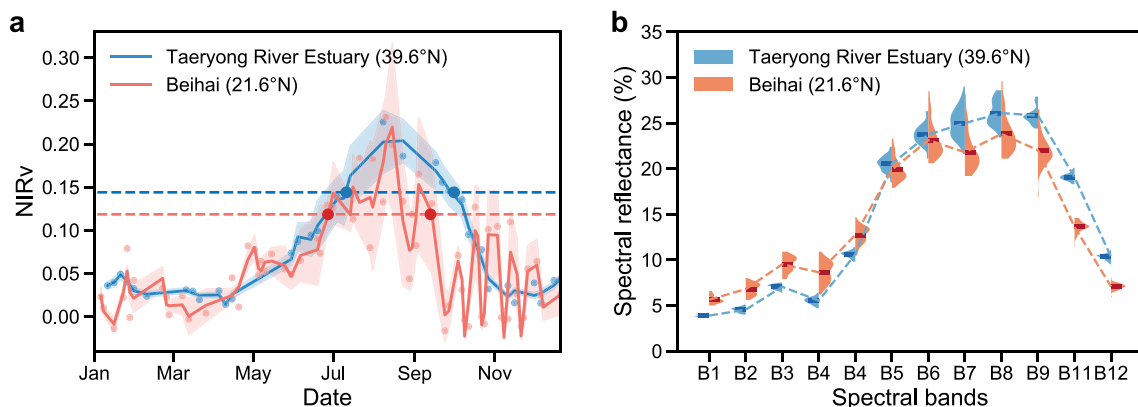


Fig. 12. Comparison of phenology features between Beihai, China (21.6°N) and Taeryong River Estuary, North Korea (39.6°N). (a) Temporal profiles of NIRv in 2020 from 100 random-collected salt marshes samples for Beihai and Taeryong River Estuary. Each profile was obtained by applying Savitzky-Golay smooth technology for showing phenological dynamics. The shaded area refers to ± 1 standard deviation. Detected starts and ends of the growing seasons using the 20% thresholding method are shown as the points. (b) Spectral characteristics of salt marshes during the detected growing seasons. The reflectance values were calculated from the median composite images of original Sentinel-2 images with NIRv value larger than top the 20% thresholds. The violins show the probability density distribution of the spectral reflectance. Horizontal lines within the violins indicate the mean spectral reflectance.

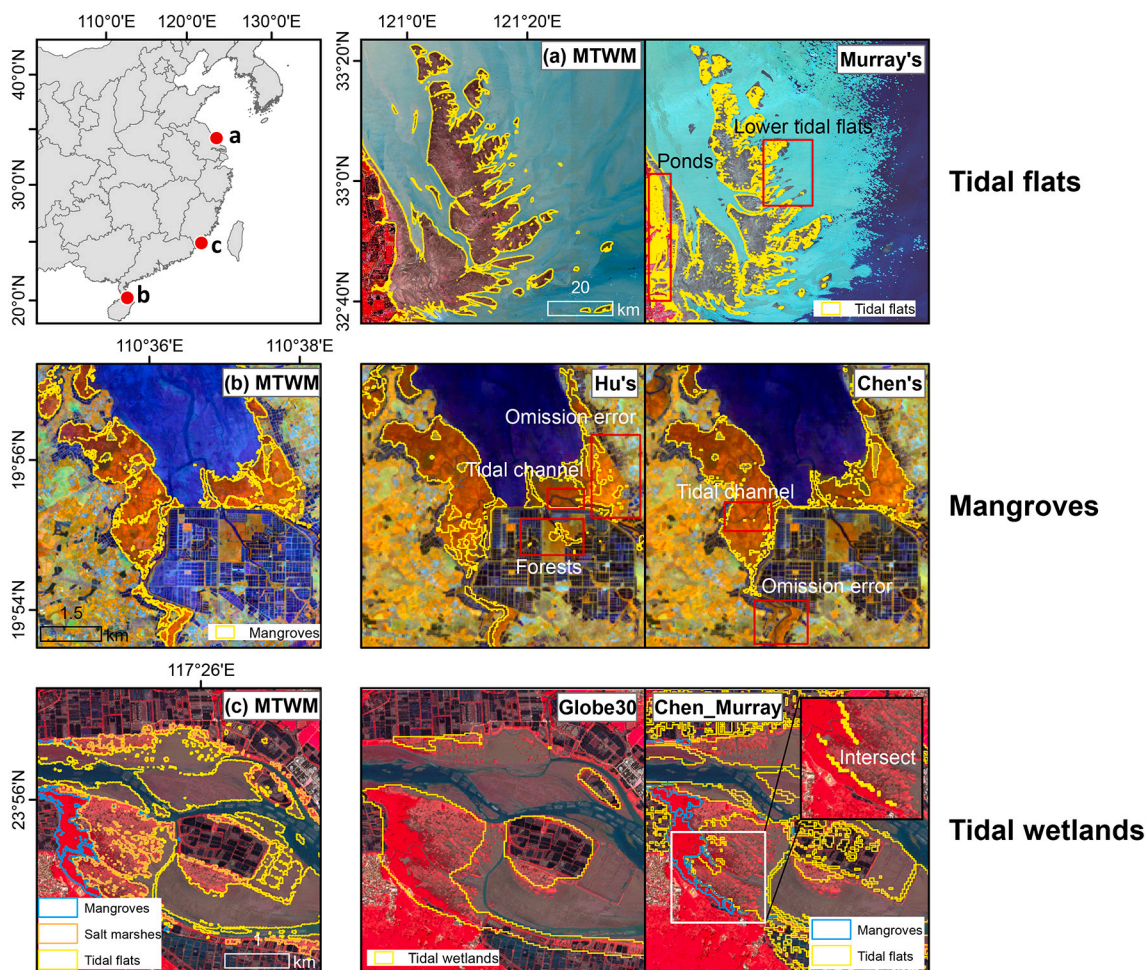


Fig. 13. Comparison of tidal wetland maps for three locations. (a) Yancheng in Jiangsu, China; (b) Dongzhai Harbor in Hainan, China; (c) Zhangjiang Estuary in Fujian, China. The yellow lines in each panel are the extracted wetland boundary of corresponding data, overlaid on a standard false colour of LETC. The background images in (b) are visualized using NIR, SWIR and Red as RGB for better visualization of mangroves. Background images in Murray_TF, Hu_MG and Chen_MG are Landsat LETC images in 2015 for matching the period of these wetland maps. Chen_Murray represents the combination of Chen_MG and Murray_TF. (For interpretation of the references to colour in this figure legend, the reader is referred to the web version of this article.)

Table 6
Area comparisons between our tidal wetland map and publicly available data.

	MTWM	Hu_MG	Chen_MG	Murray_TF	Globe30
Mangrove area (ha)	19,510.5	18,091.2	21,854.2		
Tidal flat area (ha)	1,165,888.3			1,531,069.6	
Tidal wetland area (ha)	1,308,240.8				716,140.6

4.3. Potential application and future work

Our results provide a tidal wetland composition map at 10-m spatial resolution for EA. The multiple classes and high resolution, together with the sub-continental extent of our maps, makes it useful for planners and policymakers undertaking coastal natural resources surveys and for ecologists requiring prompt and accurate information on multi-class tidal wetland cover as inputs into studies spanning a wide range of purposes, including biological invasion, coastal biogeography, biodiversity, migratory bird habitats, and blue carbon. In addition, the temperature, precipitation, and latitudinal gradients within the study area provide a natural laboratory (Frenne et al., 2013) for further studies on understanding the response of tidal wetlands to macroclimate change.

There are some potential applications of our methods in relevant studies. First, tidal extent and shorelines with different tide levels could be estimated using our image compositing methods. Similar to the extraction of the highest shoreline (i.e., MSE), we can also delineate the median high tide level, median tide level, median low tide level and lowest tide level to monitor tidal dynamics by separating water and land from MHTC, MLTC, median composite image and LETC images (Fig. 14a). Besides this, the stable statistical relationships between SIs (NDWI and NDVI) of tidal flats and actual tidal height shown in Fig. 3, combined with the delineated multiple shorelines discussed above, imply using the SIs of the tidal flats as a variable could help retrieve the intertidal topography. Additionally, although our image compositing methods were originally conceived for S2 data, they can also be used for other multi-spectral satellite data, such as Landsat and MODIS data, and thus can monitor the long-term trajectory of the sea level.

Second, the high-stand and low-stand mangroves could be separated based on the spectral difference. Because the spectral reflectance of high-stand mangroves is less affected by tides than those of low-stand mangroves (Fig. S2), we can input tide level features to the RF classifier to divide mangroves into high-stand and low-stand mangrove types. A straightforward way is to overlap the MSE on the vegetated wetland maps to detect which mangroves would be submerged by the highest tide level (Fig. 14b). This may be important for ecological researches, as the physiological traits of mangroves are highly regulated by tidal

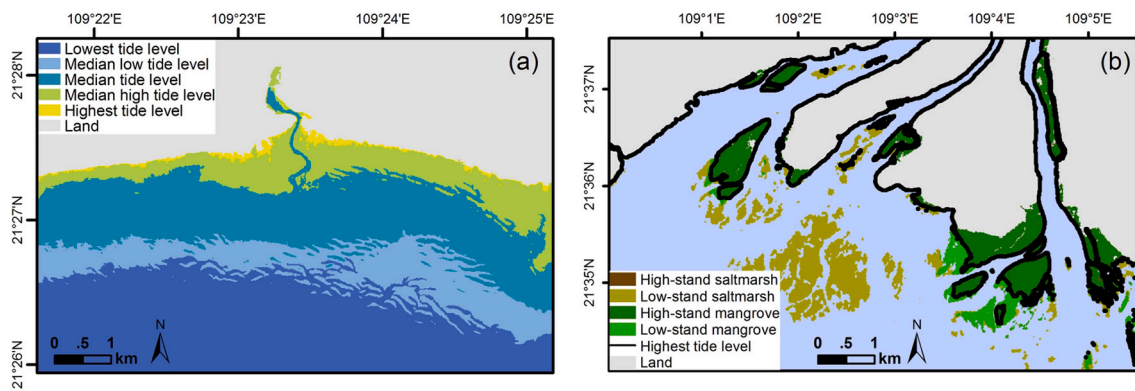


Fig. 14. Potential applications of our methods in (a) delineating shorelines under multiple tide levels and (b) distinguishing high- and low-stand mangroves and salt marshes.

flushing patterns.

The third potential application lies in applying our methods to other land-cover types. The method to composite images with different tide levels provided in this study can be extended to inland water bodies with dynamic water levels like seasonal lakes, ponds, and reservoirs. Likewise, CFGC and CFSC may also be helpful in distinguishing other vegetation types such as evergreen forests and deciduous forests, as well as croplands and grasslands.

Due to the supervised way, the main limitation in this study was the collection process of training samples. While the sensitivity test indicates MTWM-TP still performs well even with limited training samples, the hand-collecting process is still time-consuming for such a sub-continental-scale work. Recently, increasing studies (e.g., Lu and Wang, 2021; Yan and Niu, 2021) have explored automatic methods to collect training samples, but they require existing products as a reference and thus cannot be applied to land-cover types without specific existing products. Future research efforts should focus on developing fully automatic methods to collect and expand training samples. Transferring training samples from one period to another to track the temporal changes of tidal wetlands also deserves to be further explored. Additionally, MTWM-TP could be further enhanced by using start-of-the-art deep learning classifiers such as U-Net (e.g., Konapala et al., 2021) and Stacked AutoEncoder (e.g., Tian et al., 2020).

5. Conclusion

This study proposed a robust, accurate and general classification algorithm — Multi-class Tidal wetland Mapping by integrating Tide-level and Phenological features (MTWM-TP) — to overcome the challenges of tide fluctuance, cloud contamination, and spectral similarity in satellite remote sensing of tidal wetlands, demonstrating the advantage of integrating tide-level and phenological features in mapping tidal wetland composition. MTWM-TP excluded inland areas and distinguished deciduous salt marshes and evergreen mangroves by using a developed image compositing method that generates noise-free images with different tide levels and phenological stages without dependence on prior knowledge. The robustness and generality of MTWM-TP were validated across the entire coastal zone of East Asia using time-series Sentinel-2 scenes, demonstrating its ability in large-scale applications. The derived 10-m resolution multi-class tidal wetland map provides the first spatially explicit estimate of tidal wetland composition (mangroves, salt marshes, and tidal flats) for East Asia. Both quantitative accuracy assessment and visual comparisons to existing products suggest that this sub-continental-scale tidal wetland extent data achieves superior accuracy and therefore serves as an essential reference for coastal studies such as coastal ecosystem management, blue carbon restoration, and biodiversity protection. Running MTWM-TP for a long-term monitor project to detect spatiotemporal trajectory of tidal wetland composition

is planned for the next step.

Availability of data and material

The dataset of the tidal wetland composition for East Asia presented in this study is openly available at https://figshare.com/articles/dataset/Fujian_zip/14331785.

Declaration of Competing Interest

The authors declare that they have no known competing financial interests or personal relationships that could have appeared to influence the work reported in this paper.

Acknowledgements

We are grateful to Dr. Xiangzhong Luo of Department of Geography at the National University of Singapore for his valuable suggestions which improved an earlier version of the paper. Thanks to Mr. Yufeng Jiang, Miss Qian Zhang, Mr. Xinwei Wang and Mr. Md Rasel Ahmed of Xiamen University for their assistance with data processing and proof-reading. We thank the Associate Editor and three anonymous reviewers for their useful comments. This research was supported by the National Natural Science Foundation of China (NSFC) Grant No. 41976208, Programs of Science and Technology on Basic Resources Survey for the Ministry of Science and Technology of China (No. 2017FY100701) and Project supported by Innovation Group Project of Southern Marine Science and Engineering Guangdong Laboratory (Zhuhai) (No. 311021004).

Appendix A. Supplementary data

Supplementary data to this article can be found online at <https://doi.org/10.1016/j.rse.2021.112799>.

References

- Badgley, G., Field, C.B., Berry, J.A., 2017. Canopy near-infrared reflectance and terrestrial photosynthesis. *Sci. Adv.* 3, e1602244.
- Barbier, E.B., Hacker, S.D., Kennedy, C., Koch, E.W., Stier, A.C., Silliman, B.R., 2011. The value of estuarine and coastal ecosystem services. *Ecol. Monogr.* 81, 169–193.
- Bargiel, D., 2017. A new method for crop classification combining time series of radar images and crop phenology information. *Remote Sens. Environ.* 198, 369–383.
- Belgiu, M., Drăguț, L., 2016. Random forest in remote sensing: a review of applications and future directions. *ISPRS J. Photogramm. Remote Sens.* 114, 24–31.
- Bishop-Taylor, R., Sagar, S., Lymburner, L., Beaman, R.J., 2019. Between the tides: Modelling the elevation of Australia's exposed intertidal zone at continental scale. *Estuar. Coast. Shelf Sci.* 223, 115–128.
- Bunting, P., Rosenqvist, A., Lucas, R., Rebelo, L.M., Hilarides, L., Thomas, N., Hardy, A., Itoh, T., Shimada, M., Finlayson, C., 2018. The Global Mangrove Watch—a new 2010 global baseline of mangrove extent. *Remote Sens.* 10, 1669.

- Campbell, A., Wang, Y., 2018. Examining the influence of tidal stage on salt marsh mapping using high-spatial-resolution satellite remote sensing and topobathymetric lidar. *IEEE Trans. Geosci. Remote Sens.* 56 (9), 5169–5176.
- Caparros-Santiago, J.A., Rodríguez-Galiano, V., Dash, J., 2021. Land surface phenology as indicator of global terrestrial ecosystem dynamics: a systematic review. *ISPRS J. Photogramm. Remote Sens.* 171, 330–347.
- Cavanaugh, K.C., Kellner, J.R., Forde, A.J., Gruner, D.S., Parker, J.D., Rodríguez, W., Feller, I.C., 2014. Poleward expansion of mangroves is a threshold response to decreased frequency of extreme cold events. *Proc. Natl. Acad. Sci. U. S. A.* 111, 723–727.
- Chen, J., Jönsson, P., Tamura, M., Gu, Z., Matsushita, B., Eklundh, L., 2004. A simple method for reconstructing a high-quality NDVI time-series data set based on the Savitzky–Golay filter. *Remote Sens. Environ.* 91, 332–344.
- Chen, J., Ban, Y., Li, S., 2014. China: open access to earth land-cover map. *Nature* 514, 434.
- Chen, B., Xiao, X., Li, X., Pan, L., Doughty, R., Ma, J., Dong, J., Qin, Y., Zhao, B., Wu, Z., Sun, R., Lan, G., Xie, G., Clinton, N., Giri, C., 2017. A mangrove forest map of China in 2015: analysis of time series Landsat 7/8 and Sentinel-1A imagery in Google Earth Engine cloud computing platform. *ISPRS J. Photogramm. Remote Sens.* 131, 104–120.
- Coluzzi, R., Imbrenda, V., Lanfredi, M., Simoniello, T., 2018. A first assessment of the Sentinel-2 Level 1-C cloud mask product to support informed surface analyses. *Remote Sens. Environ.* 217, 426–443.
- Donato, D.C., Kauffman, J.B., Murdiyaro, D., Kurnianto, S., Stidham, M., Kanninen, M., 2011. Mangroves among the most carbon-rich forests in the tropics. *Nat. Geosci.* 4, 293–297.
- Duarte, C.M., Losada, I.J., Hendriks, I.E., Mazarrasa, I., Marbà, N., 2013. The role of coastal plant communities for climate change mitigation and adaptation. *Nat. Clim. Chang.* 3, 961–968.
- Frenne, P., Graae, B.J., Rodríguez-Sánchez, F., Kolb, A., Chabrierie, O., Decocq, G., Kort, H., de Schrijver, A., Diekmann, M., Eriksson, O., Gruwez, R., Hermy, M., Lenoir, J., Plue, J., Coomes, D.A., Verheyen, K., 2013. Latitudinal gradients as natural laboratories to infer species' responses to temperature. *J. Ecol.* 101, 784–795.
- Giri, C., Ochieng, E., Tieszen, L.L., Zhu, Z., Singh, A., Loveland, T., Masek, J., Duke, N., 2011. Status and distribution of mangrove forests of the world using earth observation satellite data. *Glob. Ecol. Biogeogr.* 20, 154–159.
- Gong, P., Liu, H., Zhang, M., Li, C., Wang, J., Huang, H., Clinton, N., Ji, L., Li, W., Bai, Y., Chen, B., Xu, B., Zhu, Z., Yuan, C., Suen, P.H., Guo, J., Xu, N., Li, W., Zhao, Y., Yang, J., Yu, C., Wang, X., Fu, H., Yu, L., Dronova, I., Hui, F., Cheng, X., Shi, X., Xiao, F., Liu, Q., Song, L., 2019. Stable classification with limited sample: transferring a 30-m resolution sample set collected in 2015 to mapping 10-m resolution global land cover in 2017. *Sci. Bull.* 64, 370–373.
- Gorelick, N., Hancher, M., Dixon, M., Ilyushchenko, S., Thau, D., Moore, R., 2017. Google Earth Engine: planetary-scale geospatial analysis for everyone. *Remote Sens. Environ.* 202, 18–27.
- Gu, J., Jin, R., Chen, G., Ye, Z., Li, Q., Wang, H., Li, D., Christakos, G., Agustí, S., Duarte, C.M., Luo, Y., Wu, J., 2021. Areal extent, species composition, and spatial distribution of coastal saltmarshes in China. *IEEE J. Select. Topics Appl. Earth Observ. Rem. Sens.* 14, 7085–7094.
- Hamilton, S.E., Casey, D., 2016. Creation of a high spatio-temporal resolution global database of continuous mangrove forest cover for the 21st century (CGMFC-21). *Glob. Ecol. Biogeogr.* 25, 729–738.
- Holben, B.N., 1986. Characteristics of maximum-value composite images from temporal AVHRR data. *Int. J. Remote Sens.* 7, 1417–1434.
- Hu, L., Li, W., Xu, B., 2018. Monitoring mangrove forest change in China from 1990 to 2015 using Landsat-derived spectral-temporal variability metrics. *Int. J. Appl. Earth Obs. Geoinf.* 73, 88–98.
- Jia, M., Wang, Z., Zhang, Y., Mao, D., Wang, C., 2018. Monitoring loss and recovery of mangrove forests during 42 years: the achievements of mangrove conservation in China. *Int. J. Appl. Earth Obs. Geoinf.* 73, 535–545.
- Jia, M., Wang, Z., Mao, D., Ren, C., Wang, C., Wang, Y., 2021. Rapid, robust, and automated mapping of tidal flats in China using time series Sentinel-2 images and Google Earth Engine. *Remote Sens. Environ.* 255, 112285.
- Kelleway, J.J., Cavanaugh, K., Rogers, K., Feller, I.C., Ens, E., Doughty, C., Saintilan, N., 2017. Review of the ecosystem service implications of mangrove encroachment into salt marshes. *Glob. Chang. Biol.* 23, 3967–3983.
- Kim, T., Kim, Y.S., Lee, H.J., 2020. Characteristics of geological lineaments along the eastern coast of the Korean peninsula: a statistical approach. *J. Coast. Res.* 102 (SI), 88–100.
- Kirwan, M.L., Walters, D.C., Reay, W.G., Carr, J.A., 2016. Sea level driven marsh expansion in a coupled model of marsh erosion and migration. *Geophys. Res. Lett.* 43 (9), 4366–4373.
- Konapala, G., Kumar, S.V., Ahmad, S.K., 2021. Exploring Sentinel-1 and Sentinel-2 diversity for flood inundation mapping using deep learning. *ISPRS J. Photogramm. Remote Sens.* 180, 163–173.
- Lopes, C.L., Mendes, R., Caçador, I., Dias, J.M., 2020. Assessing salt marsh extent and condition changes with 35 years of Landsat imagery: Tagus Estuary case study. *Remote Sens. Environ.* 247, 111939.
- Lopez-Martinez, C., Fabregas, X., 2003. Polarimetric SAR speckle noise model. *IEEE Trans. Geosci. Remote Sens.* 41, 2232–2242.
- Lovelock, C.E., Reef, R., 2020. Variable impacts of climate change on blue carbon. *One Earth* 3, 195–211.
- Lu, Y., Wang, L., 2021. How to automate timely large-scale mangrove mapping with remote sensing. *Remote Sens. Environ.* 264, 112584.
- Mao, D., Wang, Z., Du, B., Li, L., Tian, Y., Jia, M., Zeng, Y., Song, K., Jiang, M., Wang, Y., 2020. National wetland mapping in China: a new product resulting from object-based and hierarchical classification of Landsat 8 OLI images. *ISPRS J. Photogramm. Remote Sens.* 164, 11–25.
- McCarthy, M.J., Radabaugh, K.R., Moyer, R.P., Muller-Karger, F.E., 2018. Enabling efficient, large-scale high-spatial resolution wetland mapping using satellites. *Remote Sens. Environ.* 208, 189–201.
- Murray, N., Phinn, S., Clemens, R., Roelfsema, C., Fuller, R., 2012. Continental scale mapping of tidal flats across East Asia using the Landsat archive. *Remote Sens.* 4, 3417–3426.
- Murray, N.J., Phinn, S.R., DeWitt, M., Ferrari, R., Johnston, R., Lyons, M.B., Clinton, N., Thau, D., Fuller, R.A., 2019. The global distribution and trajectory of tidal flats. *Nature* 565, 222–225.
- Nicholls, R.J., Cazenave, A., 2010. Sea-level rise and its impact on coastal zones. *Science* 328 (5985), 1517–1520.
- O'Connell, J.L., Mishra, D.R., Cotten, D.L., Wang, L., Alber, M., 2017. The Tidal Marsh Inundation Index (TMII): an inundation filter to flag flooded pixels and improve MODIS tidal marsh vegetation time-series analysis. *Remote Sens. Environ.* 201, 34–46.
- Olofsson, P., Foody, G.M., Herold, M., Stehman, S.V., Woodcock, C.E., Wulder, M.A., 2014. Good practices for estimating area and assessing accuracy of land change. *Remote Sens. Environ.* 148, 42–57.
- Osland, M.J., Enwright, N.M., Day, R.H., Gabler, C.A., Stagg, C.L., Grace, J.B., 2016. Beyond just sea-level rise: considering macroclimatic drivers within coastal wetland vulnerability assessments to climate change. *Glob. Chang. Biol.* 22, 1–11.
- Pekel, J.F., Cottam, A., Gorelick, N., Belward, A.S., 2016. High-resolution mapping of global surface water and its long-term changes. *Nature* 540, 418–422.
- Pelletier, C., Valero, S., Inglada, J., Champion, N., Dedieu, G., 2016. Assessing the robustness of Random Forests to map land cover with high resolution satellite image time series over large areas. *Remote Sens. Environ.* 187, 156–168.
- Roberts, D., Mueller, N., McIntyre, A., 2017. High-dimensional pixel composites from earth observation time series. *IEEE Trans. Geosci. Remote Sens.* 55, 6254–6264.
- Rodríguez, J.D., Perez, A., Lozano, J.A., 2009. Sensitivity analysis of k-fold cross validation in prediction error estimation. *IEEE Trans. Pattern Anal. Mach. Intell.* 32 (3), 569–575.
- Rogers, K., Lymburner, L., Salum, R., Brooke, B.P., Woodroffe, C.D., 2017. Mapping of mangrove extent and zonation using high and low tide composites of Landsat data. *Hydrobiologia* 803, 49–68.
- Sagar, S., Roberts, D., Bala, B., Lymburner, L., 2017. Extracting the intertidal extent and topography of the Australian coastline from a 28 year time series of Landsat observations. *Remote Sens. Environ.* 195, 153–169.
- Saintilan, N., Wilson, N.C., Rogers, K., Rajkaran, A., Krauss, K.W., 2014. Mangrove expansion and salt marsh decline at mangrove poleward limits. *Glob. Chang. Biol.* 20, 147–157.
- Simard, M., Fatoyinbo, L., Smetanka, C., Rivera-Monroy, V.H., Castañeda-Moya, E., Thomas, N., van der Stocken, T., 2019. Mangrove canopy height globally related to precipitation, temperature and cyclone frequency. *Nat. Geosci.* 12, 40–45.
- Stehman, S.V., Foody, G.M., 2019. Key issues in rigorous accuracy assessment of land cover products. *Remote Sens. Environ.* 231, 111199.
- Sun, C., Li, J., Liu, Y., Liu, Y., Liu, R., 2021. Plant species classification in salt marshes using phenological parameters derived from Sentinel-2 pixel-differential time-series. *Remote Sens. Environ.* 256, 112320.
- Taddeo, S., Dronova, I., Depsky, N., 2019. Spectral vegetation indices of wetland greenness: responses to vegetation structure, composition, and spatial distribution. *Remote Sens. Environ.* 234, 111467.
- Tadono, T., Takaku, J., Tsutsui, K., Oda, F., Nagai, H., 2015. Status of ALOS World 3D (AW3D) global DSM generation. In: *IEEE International Geoscience and Remote Sensing Symposium*, pp. 3822–3825.
- Tian, J., Wang, L., Yin, D., Li, X., Diao, C., Gong, H., Shi, C., Menenti, M., Ge, Y., Nie, S., Ou, Y., Song, X., Liu, X., 2020. Development of spectral-phenological features for deep learning to understand *Spartina alterniflora* invasion. *Remote Sens. Environ.* 242, 111745.
- Turpie, K.R., Klemas, V.V., Byrd, K., Kelly, M., Jo, Y.H., 2015. Prospective HyspIRI global observations of tidal wetlands. *Remote Sens. Environ.* 167, 206–217.
- Valderrama-Landeros, L., Flores-Verdugo, F., Rodríguez-Sobeyra, R., Kovacs, J.M., Flores-de-Santiago, F., 2021. Extrapolating canopy phenology information using Sentinel-2 data and the Google Earth Engine platform to identify the optimal dates for remotely sensed image acquisition of semiarid mangroves. *J. Environ. Manag.* 279, 111617.
- Wang, L., Jia, M., Yin, D., Tian, J., 2019. A review of remote sensing for mangrove forests: 1956–2018. *Remote Sens. Environ.* 231, 111223.
- Wang, X., Xiao, X., Zou, Z., Hou, L., Qin, Y., Dong, J., Doughty, R.B., Chen, B., Zhang, X., Chen, Y., Ma, J., Zhao, B., Li, B., 2020. Mapping coastal wetlands of China using time series Landsat images in 2018 and Google Earth Engine. *ISPRS J. Photogramm. Remote Sens.* 163, 312–326.
- White, M.A., de Beurs, K.M., Didan, K., Inouye, D.W., Richardson, A.D., Jensen, O.P., O'Keefe, J., Zhang, G., Nemani, R.R., van Leeuwen, W.J.D., Brown, J.F., de Wit, A., de Schaepman, M., Lin, X., Dettlinger, M., Bailey, A.S., Kimball, J., Schwartz, M.D., Baldocchi, D.D., Lee, J.T., Lauenroth, W.K., 2009. Intercomparison, interpretation, and assessment of spring phenology in North America estimated from remote sensing for 1982–2006. *Glob. Chang. Biol.* 15, 2335–2359.
- Xu, P., Herold, M., Tsensbazar, N.-E., Clevers, J.G., 2020. Towards a comprehensive and consistent global aquatic land cover characterization framework addressing multiple user needs. *Remote Sens. Environ.* 250, 112034.
- Yan, X., Niu, Z., 2021. Reliability evaluation and migration of wetland samples. *IEEE J. Select. Topics Appl. Earth Observ. Rem. Sens.* 14, 8089–8099.

- Yang, S.L., Li, H., Ysebaert, T., Bouma, T.J., Zhang, W.X., Wang, Y.Y., Li, P., Li, M., Ding, P.X., 2008. Spatial and temporal variations in sediment grain size in tidal wetlands, Yangtze Delta: on the role of physical and biotic controls. *Estuar. Coast. Shelf Sci.* 77 (4), 657–671.
- Zeng, L., Wardlow, B.D., Xiang, D., Hu, S., Li, D., 2020. A review of vegetation phenological metrics extraction using time-series, multispectral satellite data. *Remote Sens. Environ.* 237, 111511.
- Zhang, X., Liu, L., Chen, X., Gao, Y., Xie, S., Mi, J., 2020. GLC_FCS30: global land-cover product with fine classification system at 30 m using time-series Landsat imagery. *Earth Syst. Sci. Data* 13 (6), 2753–2776.
- Zhao, C., Qin, C., Teng, J., 2020. Mapping large-area tidal flats without the dependence on tidal elevations: A case study of Southern China. *ISPRS J. Photogramm. Remote Sens.* 159, 256–270.
- Zhu, Z., Wang, S., Woodcock, C.E., 2015. Improvement and expansion of the Fmask algorithm: cloud, cloud shadow, and snow detection for Landsats 4–7, 8, and Sentinel 2 images. *Remote Sens. Environ.* 159, 269–277.